

RESEARCH

Open Access



# Multifunctional nanocomposites DDM<sup>plus</sup>AF inhibit the proliferation and enhance the radiotherapy of breast cancer cells via modulating tumor-promoting factors and metabolic reprogramming

Noura M. Thabet<sup>1\*</sup>, Mohamed K. Abdel-Rafei<sup>1</sup>, Ghariieb S. El-Sayyad<sup>2</sup>, Mohamed Abd Elkodous<sup>3</sup>, Adel Shaaban<sup>4,5,6</sup>, Yi-Chun Du<sup>5,6\*</sup>, Laila Ahmed Rashed<sup>7</sup> and Mostafa A. Askar<sup>1</sup>

\*Correspondence:  
noura\_magdy@hotmail.com;  
terrydu@gs.ncku.edu.tw

<sup>1</sup> Radiation Biology Department, National Centre for Radiation Research and Technology (NCRRT), Egyptian Atomic Energy Authority (EAEA), Cairo, Egypt  
<sup>5</sup> Department of Biomedical Engineering, National Cheng Kung University, Tainan 70105, Taiwan  
Full list of author information is available at the end of the article

## Abstract

**Background:** Tumor-promoting factors (TPF) and metabolic reprogramming are hallmarks of cancer cell growth. This study is designed to combine the newly synthesized two nanocomposites DDM (HA-FA-2DG@DCA@MgO) and AF (HA-FA-Amygdaline@Fe<sub>2</sub>O<sub>3</sub>) with fractionated doses of radiotherapy (6 Gy-FDR; fractionated dose radiotherapy) to improve the efficiency of chemo-radiotherapy against breast cancer cell lines (BCCs; MCF-7 and MDA-MB-231). The physicochemical properties of each nanocomposite were confirmed using energy dispersive XRD, FTIR, HR-TEM, and SEM. The stability of DDM<sup>plus</sup>AF was also examined, as well as its release and selective cellular uptake in response to acidic pH. A multiple-MTT assay was performed to evaluate the radiosensitivity of BCCs to DDM<sup>plus</sup>AF at 3 Gy (single dose radiotherapy; SDR) and 6 Gy-FDR after 24, 48, and 72 h. Finally, the anti-cancer activity of DDM<sup>plus</sup>AF with 6 Gy-FDR was investigated via assessing the cell cycle distribution and cell apoptosis by flow cytometry, the biochemical mediators (HIF-1 $\alpha$ , TNF- $\alpha$ , IL-10, P53, PPAR- $\alpha$ , and PRMT-1), along with glycolytic pathway (glucose, HK, PDH, lactate, and ATP) as well as the signaling effectors (protein expression of AKT, AMPK, SIRT-1, TGF- $\beta$ , PGC-1 $\alpha$ , and gene expression of ERR- $\alpha$ ) were determined in this study.

**Results:** The stability of DDM<sup>plus</sup>AF was verified over 6 days without nanoparticle aggregation. DDM<sup>plus</sup>AF release and selectivity data revealed that their release was amenable to the acidic pH of the cancer environment, and their selectivity was enhanced towards BCCs owing to CD44 and FR- $\alpha$  receptors-mediated uptake. After 24 h, DDM<sup>plus</sup>AF boosted the BCC radiosensitivity to 6 Gy-FDR. Cell cycle arrest (G2/M and pre-G1), apoptosis induction, modulation of TPF mediators and signaling effectors, and suppression of aerobic glycolysis, all confirmed DDM<sup>plus</sup>AF + 6 Gy's anti-cancer activity.



**Conclusions:** It could be concluded that DDM<sup>Plus</sup>AF exerted a selective cancer radiosensitizing efficacy with targeted properties for TPF and metabolic reprogramming in BCCs therapy.

**Keywords:** Nanocomposites, Targeted therapy, Radiotherapy, TPF, Metabolic reprogramming, Glycolysis

## Background

Breast cancer (BC) is the most common malignancy in women and one of the three most common cancers worldwide, along with lung and colon cancer (Harbeck and Gnant 2017). Adenosine triphosphate (ATP; energy source for survival) is produced in normal cells via two pathways: glycolysis and mitochondrial oxidative phosphorylation (OXPHOS). However, even in an aerobic environment, cancer cells gain ATP from glycolysis rather than OXPHOS, despite the glycolysis producing 2 ATP less than the OXPHOS that generates 36 ATP per glucose molecule. Notably, mitochondrial OXPHOS is not necessarily defective in cancer cells, but cancer cells mostly depend on glycolysis due to its acceleration than OXPHOS in ATP generation, and this is favorable for growth and proliferation. This metabolic reprogramming is recognized as the Warburg effect, and it is the cancer hallmark that is induced by oncogenic events and aggressively contributes to cancer progression in a harsh microenvironment (Dias et al. 2019; Shiratori et al. 2019).

The tumor microenvironment (TME) is an immunosuppressive microenvironment generated by cancer cells to regulate tumor growth, promote tumor immune evasion, and serve as a source of tumor-promoting factors (TPF) (Whiteside 2008; Shi et al. 2020). TPF has included growth factors, cytokines, extracellular matrix proteins, and hypoxia challenge as well as p53, which promote growth, survival, and metastatic spread of cancer cells (Han et al. 2014; Owusu et al. 2017). The TME is the network of cells such as immune cells, cancer-associated fibroblasts, and promoting factors (i.e., cytokines, growth factors, and hormones) associated with the extracellular matrix and surrounding vasculature that encloses cancer cells. The formation of this TME essentially relies on tumor metabolism, and therefore, it is characterized by high acidity and hypoxia (Shi et al. 2020). Additionally, the study by Vaughan et al. (2013) demonstrated that aerobic glycolysis is induced by the expression of oncogene and TME mediators. Furthermore, aerobic glycolysis leads to the accumulation of lactate in the TME, which results in stabilization of hypoxia-inducible factor (HIF), and subsequently stimulates transforming growth factor- $\beta$  (TGF- $\beta$ ) that in turn enhances aerobic glycolysis (Hua et al. 2020). Moreover, among the numerous regulators or mediators of cancer metabolism, peroxisome proliferator-activated receptor- $\gamma$  coactivator-1  $\alpha$  (PGC-1 $\alpha$ ) is emerging as a promoter of carcinogenesis and an essential controller of multiple metabolic pathways in cancer (Tan et al. 2016). Notably, PGC-1 $\alpha$  is controlled by several post-translational modifications. Because PGC-1 $\alpha$  is markedly sensitive to cellular energy status, it is tightly regulated by stress sensors such as AMP activated protein kinase (AMPK) and sirtuin-1 (SIRT-1) that activate PGC-1 $\alpha$  under energy deprivation conditions (Tan et al. 2016). Protein arginine methyltransferases-1 (PRMT-1), one of nine PRMTs, catalyzes arginine methylation that is known to have a role in cell proliferation and survival, transformation,

signal transduction, resistance to DNA damaging agents and invasion in breast, colon, lung cancer and so on (Baldwin et al. 2014).

Nowadays, a promising strategy in cancer therapy has been observed through the combination of multiple drugs, such as chemotherapeutic drugs in combination with radiotherapy, based on the synergistic effect of multiple drugs with gamma radiation. In the current study, DDM<sup>plus</sup>AF comprised two nanocomposites of DDM (HA-FA-2DG@DCA@MgO) and AF (HA-FA-Amygdaline@Fe<sub>2</sub>O<sub>3</sub>), which are used as combination for cancer therapy. Noteworthy, the DDM in the nano-core-shell structure is constituted of 2-deoxy-D-glucose (2-DG), an inhibitor of glycolysis because it is an analogue structure of glucose that is phosphorylated with hexokinase (HK) irreversibly into 2DG-phosphate and leads to blocked ATP production via glycolysis (Pyaskovskaya et al. 2016). Meanwhile, sodium dichloroacetate (DCA), by blocking pyruvate dehydrogenase (PDH) kinase (PDK), promotes a shifting of tumor cell metabolism from glycolysis to OXPHOS (Pyaskovskaya et al. 2016). AF, on the other hand, is made up of amygdalin, a naturally occurring vitamin B-17 found in the seeds of many *Prunus Rosacea* family plants (apricot, apples, bitter almond, black cherries, plums, and peach). The chemical structure of amygdalin consists of benzaldehyde, hydrocyanic acid, and D-mandelonitrile-β-D-glucoside-6-β-glucoside (2-glucose molecules) (Liczbiński and Bukowska 2018). Amygdalin acts as an anti-cancer agent by inducing apoptosis and cell cycle arrest, which depends mainly on releasing toxic hydrogen cyanide (HCN) only in cancer cells after it has been hydrolyzed and destroys them. Unfortunately, HCN also reaches normal cells and is not safe for humans (Liczbiński and Bukowska 2018; El-Desouky et al. 2020). Hyaluronic acid (HA) and folic acid (FA) are known as drug carriers that improve the targeting efficiency in cancer therapy due to their properties such as requisite nutrient, good stability, non-toxicity, and biodegradability by TPF and allow the release of anti-cancer drugs at the disease site (Liu et al. 2019; Jurczyk et al. 2021). HA and FA enter cancer cells by binding to CD44 receptor and folate receptor-α (FR-α), respectively, indicating their selectivity for cancer cells over normal cells. CD44 and FR-α receptors are known to be over-expressed in breast cancer cells (BCCs) and have a high affinity for HA and FA, which are typically captured to feed by the fast-dividing BCCs (Liu et al. 2019). Interestingly, it was found that different metal oxide nanoparticles induce cytotoxicity in cancer cells, but not in normal cells, through the generation of reactive oxygen species (ROS), induction of apoptosis and necrosis, and by evoking a pro- or anti-inflammatory mediator to optimize the immune function for the antitumor response (Vinardell and Mitjans 2015; Dukhinova et al. 2019). In particular, magnesium oxide (MgO) and iron oxide nanoparticles (IO-NPs; Fe<sub>2</sub>O<sub>3</sub>) have attracted great attention in cancer therapy. MgO-NPs have recently demonstrated multi-potential activity in drug delivery, anti-cancer, radiosensitization, magnetic resonance imaging (MRI), and hyperthermia systems, and their incorporation in nanomaterials could aid in drug uptake tracking via TEM imaging. In the fabrication of nanoparticles, MgO can also be used in the core of nanomaterials to form a regular crystal and produce the face-centered cubic (FCC) crystalline configuration (Abdel Maksoud et al. 2018; Behzadi et al. 2019). Moreover, IO-NPs have proven ideal as negative T2 magnetic resonance imaging (MRI) contrast agents (Mi et al. 2016). In addition, IO-NPs are regarded as ideal agents for cancer diagnosis, treatment, and treatment monitoring due to their excellent properties such as facile

synthesis, biocompatibility, and biodegradability (Revia and Zhang 2016). Owing to their ability to augment the cytotoxic effects of  $\gamma$ -radiation, IO-NPs have potential applications in photothermal therapy (PTT), photodynamic therapy (PDT), magnetic hyperthermia, and chemo/biotherapeutics (Espinosa et al. 2016; Cazares-Cortes et al. 2017), as well as promising radiosensitizers/enhancers (Mazur et al. 2013). Besides the above, radiotherapy is a main and fundamental component in the management of cancer. Irradiation not only destroys the structure of the DNA double helix

, which activates the induction of apoptosis, necrosis, and affects normal mitosis events, but it also interferes with the regulation of cell signaling pathways, which leads to changes in the immunogenicity and microenvironment of neoplastic cells (Wang et al. 2018).

Therefore, based on the above, this study is designed to incorporate HA-FA as dual-targeting with core-shell nanoparticles DDM<sup>Plus</sup>AF for cancer therapy. This is achieved through investigating the selectivity and anti-cancer effect of DDM<sup>Plus</sup>AF with radiotherapy to target the TPF and metabolic reprogramming of cancer cells through evaluating the TPF mediators (HIF-1 $\alpha$ , TNF- $\alpha$ , IL-10, P53, PPAR- $\alpha$ , and PRMT-1), glycolytic pathways (glucose, HK, PDH, lactate, and ATP) and regulators of cancer metabolism (protein expression of AKT, AMPK, SIRT-1, TGF- $\beta$ , PGC-1 $\alpha$  and gene expression of ERR- $\alpha$ ) in BCCs.

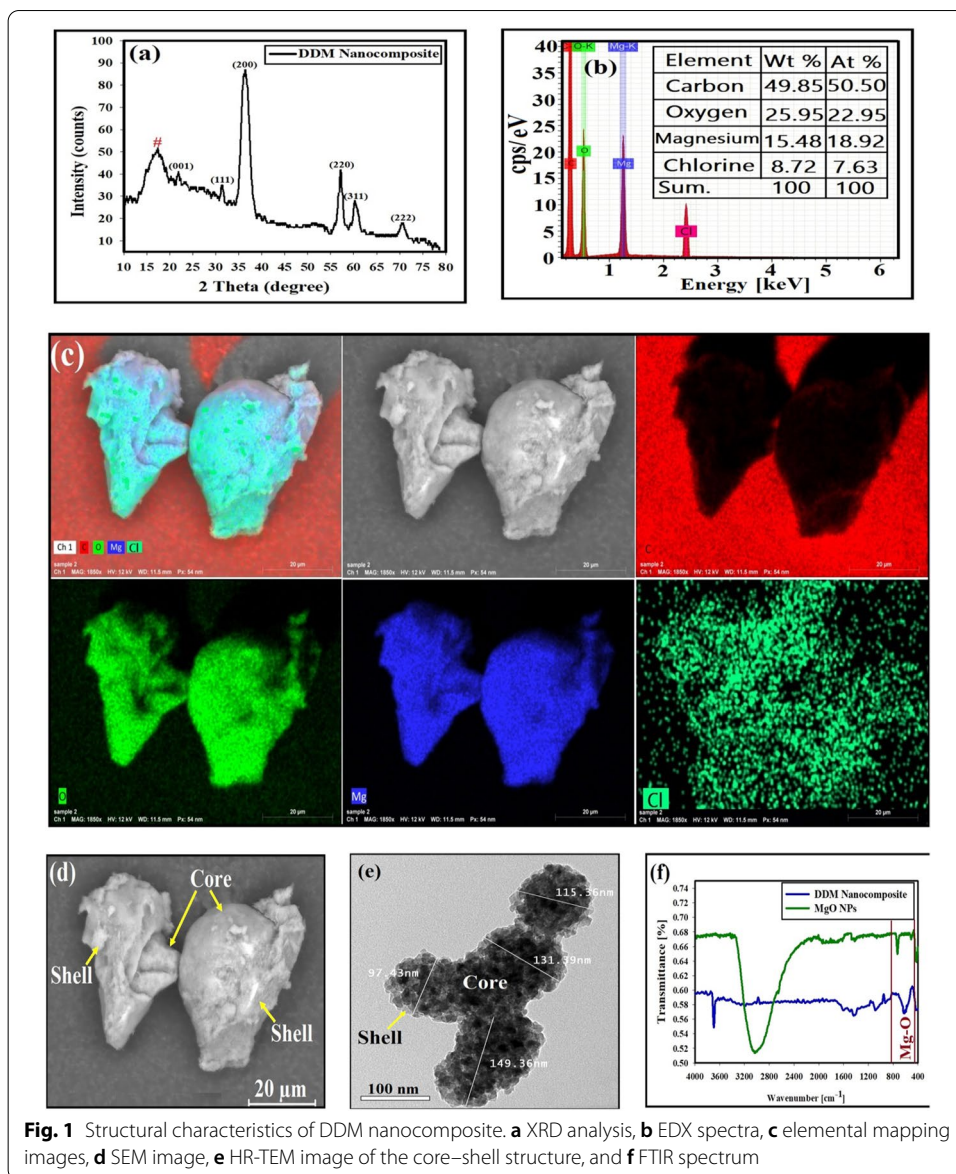
## Results

### Characterization of DDM (HA-FA-2DG@DCA@MgO)

The XRD displayed a true detection of the crystallinity and the combination of the exposed DDM sample, because it explains the status of the atoms, size, and axes. The XRD results of the DDM powder are presented in Fig. 1a; many peaks were recognized for MgO-NPs. Diffraction characteristics were displayed inside  $2\theta$  (degree) as 21.83, 31.31, 36.40, 57.04, 60.10 and 70.42 where some peaks represent the Bragg's appearances (001), (111), (20), (220), (311), and (222) extensions in that position sequentially, which could be recorded to the levels of cubic MgO (JCPDS 75-0447). This proves that the MgO-NPs (core) crystallized in a regular manner, resulting in the face-centered cubic (FCC) crystalline structure. It must be noted that the amorphous peak at 17.26 ( $\theta$ ) was caused by outer organic shells (DCA, 2DG, HA, and FA), indicating the successful formation of core-shell construction.

The composition of the synthesized DDM sample is analyzed by EDX (Fig. 1b), where the presence of O, C, Cl, and Mg was confirmed, and the presence of Mg and O atoms was correlated to the core MgO-NPs. Moreover, the presence of O, C, and Cl corresponds to the DA, 2DG, HA, and FA multi-shell structures in the synthesized sample.

Elemental mappings were performed selectively on the synthesized DDM samples to further illustrate the core-shell structural features of the samples, and the images are depicted in Fig. 1c. These images demonstrated the existence of the elements Mg, C, Cl, and O, which agreed with the preceding EDX results. Furthermore, those elements were distributed uniformly. The images confirmed that both Mg (blue color) and O (green color) atoms were located in the same places, confirming the core structure, and the



other layers (C, O, and Cl) indicate the distribution of the organic shells structure on the core MgO-NPs.

The SEM image of the synthesized DDM sample is shown in Fig. 1d. The surface behavior reveals dark layers that represent the outer shells (HA and FA; organic shells) with remarkable smooth agglomerates. This could be due to the occupation of a large number of layers at the grain boundary, which could control the grain growth. In addition, the MgO-NPs in the core represented the bright aggregate particles, confirming the promising core-shell structure.

An HR-TEM image of the core-shell structure of the synthesized DDM is shown in Fig. 1e. The synthesized composite possessed a semi-spherical structure with diameter sizes ranging from 149.36 to 97.43 nm, with an average size of 123.38 nm. It must be noted that the condensed particles were attributed to the core MgO-NPs while the

faint layers corresponded to the shell layers of DDM, which were entirely validated by color in the mapping/SEM images and indicated the successful formation of core-shell construction.

The FTIR spectrum of the synthesized DDM is presented in Fig. 1f. For the current nanocomposite, the characteristic vibration peak at  $680\text{ cm}^{-1}$  was assigned to the stretching mode of MgO (in the core) and other assigned peaks for the shells were formed and were in good agreement with the literature. After conducting a comparative FTIR analysis of bare MgO-NPs, a peak located at  $3040\text{ cm}^{-1}$  was assigned to the -OH stretching region. Another peak located at  $731\text{ cm}^{-1}$  was appointed to the stretching mode of the Mg-O core, which slightly shifted as compared with Mg-O in the synthesized nanocomposite due to the absence of organic shells. After the FTIR conduct of the bare MgO-NPs and the confirmation of the functional groups' presence as represented in the synthesized nanocomposite, the formation of core-shell construction was successfully indicated. The literature comparison was achieved between the FTIR data of bare FA (Mohammed 2014), HA (Reddy and Karunakaran 2013), DCA (Yang et al. 2018), 2DG (Jin et al. 2019), and bare MgO-NPs (Balakrishnan et al. 2020). It must be noted that the connection type between the outer organic shells and the chemical reactions on the surface of MgO-NPs was by intramolecular hydrogen bonding (weak bond) as described before, which was not present in bare FA, HA, DCA, 2DG, and bare MgO-NPs that indicated the incorporation behavior between outer layers (FA, HA, DCA, and 2DG) as indicated by a weak bond as described in recent publications (El-Batal et al. 2022). On the other hand, broadband and the change presented at  $3725\text{ cm}^{-1}$  in the case of the synthesized DDM (Fig. 1f) is related to the presence of hydroxyl groups and is attributed to OH-stretching, and was changed in the case of bare MgO-NPs ( $3040\text{ cm}^{-1}$ ), which indicates the formation of intermolecular hydrogen bonding between FA, HA, DCA, 2DG, and the synthesized core MgO-NPs. The incorporation behavior was detected in our FTIR results as new peaks formed in the nanocomposite that were not present in bare MgO-NPs as a minor shifting in the bare peaks (weak physical bond; Van der Waals forces) (Uppuluri et al. 2000; Bonn and Hunger 2021).

#### Characterization of AF (HA-FA-Amygdaline@Fe<sub>2</sub>O<sub>3</sub>)

The XRD diffractogram of the synthesized HA-FA-Amygdaline@Fe<sub>2</sub>O<sub>3</sub> sample showed a high-degree hematite (Fe<sub>2</sub>O<sub>3</sub>) in the core. An XRD system was conducted to study the crystal composition and state of the incorporated Fe<sub>2</sub>O<sub>3</sub> NPs (Fig. 2a). The XRD models agree with the specific Fe<sub>2</sub>O<sub>3</sub> original (JCPDS No. 33-0664). The unique peaks was looked at the next  $2\theta$  at  $24.18^\circ$ ,  $33.16^\circ$ ,  $35.55^\circ$ ,  $40.69^\circ$ ,  $49.42^\circ$ ,  $54.19^\circ$ ,  $57.49^\circ$ ,  $62.19^\circ$ , and  $64.18^\circ$  corresponding to 012, 104, 110, 113, 024, 116, 018, 214, and 300 planes, respectively, and showing its standard cubic spinel composition (Karade et al. 2019). There are no unknown crystalline phases or impurities in the Fe<sub>2</sub>O<sub>3</sub> NPs, which represent a high concentration in the core. This matches with the unique composition of the complete Fe<sub>2</sub>O<sub>3</sub> crystal with a rhombohedral centered hexagonal building (R3c space system) (Sharma 2017; Zeng et al. 2017; Fouad et al. 2019; Tadic et al. 2019; Liang et al. 2020). The most important diffraction peak near  $35.60^\circ$  implies that (110) facets remain the dominant  $\alpha$ -Fe<sub>2</sub>O<sub>3</sub> crystal construction. Finally, the amorphous peak at  $17.05^\circ$  (\*) was due

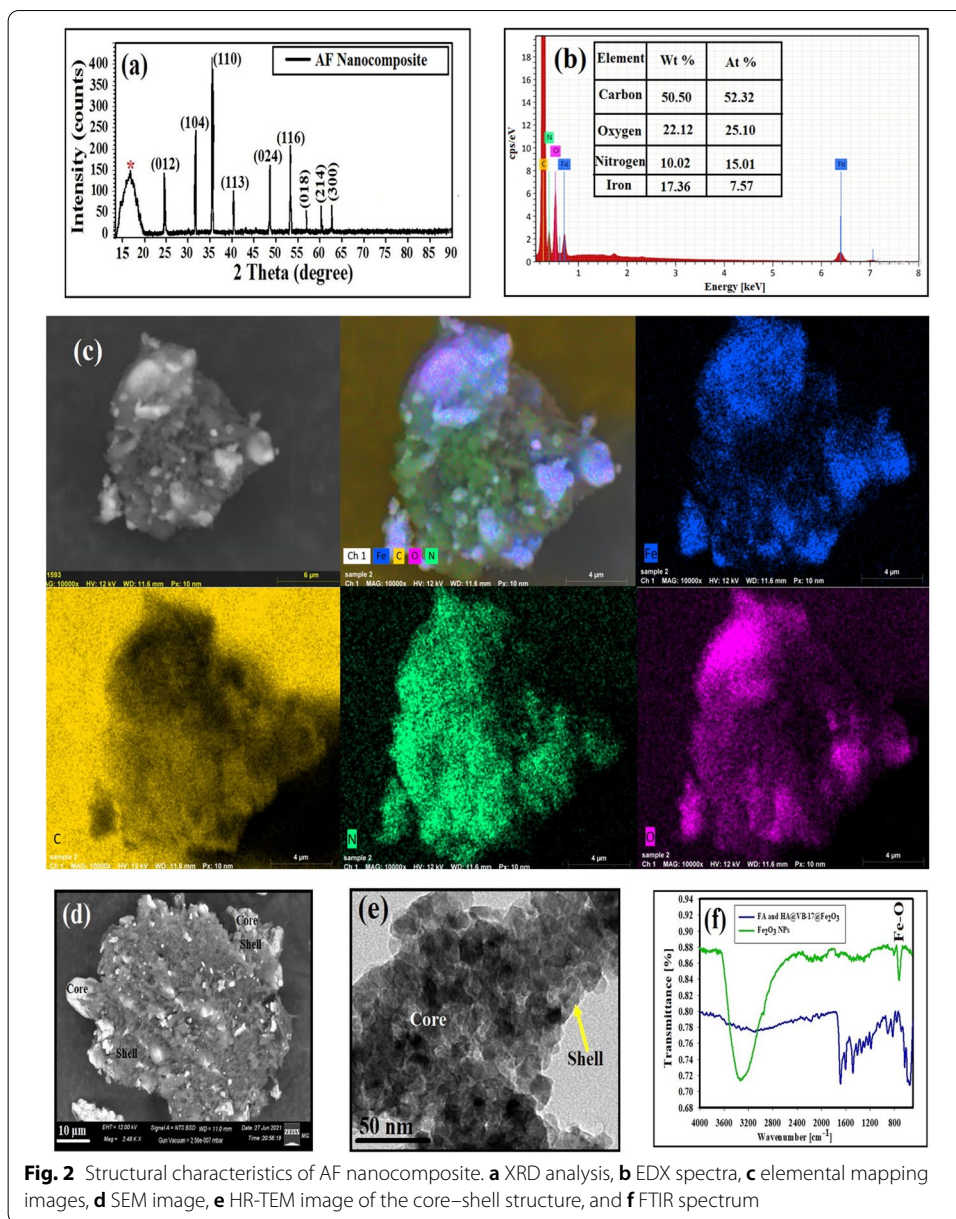


**Fig. 2** Structural characteristics of AF nanocomposite. **a** XRD analysis, **b** EDX spectra, **c** elemental mapping images, **d** SEM image, **e** HR-TEM image of the core-shell structure, and **f** FTIR spectrum

to outer organic shells (B17, HA, and FA), which indicated the successful formation of core-shell construction.

The composition of the synthesized HA-FA-Amygdaline@Fe<sub>2</sub>O<sub>3</sub> sample is analyzed by EDX (Fig. 2b), where the presence of O, C, N, and Fe was confirmed, where the existence of Fe, and O atoms was confirmed for the core Fe<sub>2</sub>O<sub>3</sub> NPs. Moreover, the presence of O, C, N, was attributed to the B-17, FA, and HA multi-shell structures in the synthesized sample (Ashour et al. 2018; Abdel Maksoud et al. 2018; Maksoud et al. 2019). In order to further illustrate the structural features of the samples, elemental mappings have been carried out selectively on the synthesized HA-FA-Amygdaline@Fe<sub>2</sub>O<sub>3</sub> and the images are depicted in Fig. 2c. It was evident from these images that the elements Fe, C, N and

O existed, which agreed with the preceding EDX results. Furthermore, those elements were homogeneously distributed. From the images, it could be concluded that both Fe and O atoms were located in the same places, which confirms the core structure.

The SEM images of the synthesized HA-FA-Amygdaline@Fe<sub>2</sub>O<sub>3</sub> are shown in Fig. 2d. The surface behavior was shown as dark layers that confirm the outer shells (B-17, FA and HA) with remarkable smooth agglomerates that could be observed due to the occupation of a large quantity of layers at the grain boundary, which could control the grain growth (Zipare et al. 2018). Also, the bright particles represented the Fe<sub>2</sub>O<sub>3</sub> NPs in the core, which confirms the promising core-shell structure.

An HR-TEM image of the core-shell structure of the synthesized HA-FA-Amygdaline@Fe<sub>2</sub>O<sub>3</sub> is shown in Fig. 2e. The synthesized composite possesses semi-spherical structure with diameter sizes ranging from 155.55 to 98.58 nm, with an average size of 111.95 nm. It must be noted that the condensed particles were attributed to the core Fe<sub>2</sub>O<sub>3</sub> NPs while the faint layers corresponded to the shell layers (B-17, FA, and HA), which were entirely validated by color in mapping/SEM images.

The data represented in Fig. 2f show the FTIR spectra of the synthesized HA-FA-Amygdaline@Fe<sub>2</sub>O<sub>3</sub>, and bare Fe<sub>2</sub>O<sub>3</sub> NPs samples. For the present nanocomposite (HA-FA-Amygdaline@Fe<sub>2</sub>O<sub>3</sub>), the characteristic vibration peak at 637 cm<sup>-1</sup> was assigned to the stretching mode of Fe-O (in the core) and was in a good agreement with the literature (Shebanova and Lazor 2003; Luo et al. 2020), and a noted peak located 726 cm<sup>-1</sup> in the synthesized bare Fe<sub>2</sub>O<sub>3</sub> NPs indicated a finger print for Fe-O. At the same time, a broad peak assigned at 3333 cm<sup>-1</sup> (bare Fe<sub>2</sub>O<sub>3</sub> NPs) was assigned to O-H group from water molecules.

In the FTIR results, the characteristic IR absorption peaks at 1608, 1691 and 1562 cm<sup>-1</sup> were observed in the spectrum, which was assigned to folic acid due to N-H bending vibration of CONH group, C=O amide stretching of the  $\alpha$ -carboxyl group, and the absorption band of phenyl ring, respectively (He et al. 2009). The presence of a band at 3101 cm<sup>-1</sup> was attributed to OH and NH stretching regions. The band at 2469 cm<sup>-1</sup> could be attributed to the stretching vibration of C-H in HA. The band at about 1691 cm<sup>-1</sup> corresponds to the amide carbonyl and the band at 1486 cm<sup>-1</sup> could be attributed to the stretching of COO-, which refers to the acid group of molecule HA. The absorption band at 1044 cm<sup>-1</sup> was attributed to the linkage stretching of C-OH in HA (de Oliveira et al. 2017).

Infrared spectra of vitamin B 17 were indicated by the presence of narrow peak bands at 1859 cm<sup>-1</sup> attributed to aldehyde and ketone C=O stretching (Thakur et al. 2019). The position of the C=O stretching indicated the hydrogen bonding and incorporation within the molecules (Nasser et al. 2021). High-intensity peak followed by peak at 2964 cm<sup>-1</sup> and 2873 cm<sup>-1</sup> attributed to O-H stretching (carboxylic acid) vibrations and aldehyde C-H stretching. These O-H stretching vibrations might be due to carboxylic compounds in the polymer protein matrix. Finally, the absorption bands at 1493 cm<sup>-1</sup>, 1417 cm<sup>-1</sup>, and 770 cm<sup>-1</sup> are assigned to amide II, amide III, and amide IV (Garg et al. 2007).

After the literature comparison achieved between the FTIR data of bare FA (Mohammed 2014), HA (Reddy and Karunakaran 2013), V B17 (Jaszczak-Wilke et al. 2021), and bare Fe<sub>2</sub>O<sub>3</sub> NPs (Azmat et al. 2020), it is worth mentioning that the connection type

between the outer organic shells and the chemical reactions on the surface of  $\text{Fe}_2\text{O}_3$  NPs was by intramolecular hydrogen bonding (weak bond) as described previously, which was not present in bare FA, HA, amygdalin, and bare  $\text{Fe}_2\text{O}_3$  NPs that indicated the incorporation behavior between the outer layers (FA, HA, and amygdalin) as indicated by a weak bond as described in recent publications (El-Batal et al. 2022). In our FTIR results, the incorporation behavior was detected as new peaks formed in the synthesized nanocomposite and not present in bare  $\text{Fe}_2\text{O}_3$  NPs as a minor shifting in the bare peaks (weak physical bond; Van der Waals forces) (Uppuluri et al. 2000; Bonn and Hunger 2021). On the other hand, broadband and the change presented at  $3200\text{ cm}^{-1}$  in the case of the synthesized AF (Fig. 2f) is related to the presence of hydroxyl groups and is attributed to OH-stretching, and was changed in the case of bare  $\text{Fe}_2\text{O}_3$  NPs ( $3333\text{ cm}^{-1}$ ), which indicates the formation of intermolecular hydrogen bonding between HA, FA, Amygdaline, and the synthesized core  $\text{Fe}_2\text{O}_3$  NPs.

### Cytotoxicity assay

After 24 h, the anti-cancer effects of both DDM and AF on BCCs (MCF-7 and MDA-MB-231) revealed an anti-proliferative activity against the cancer cell lines (Fig. 3). The  $\text{IC}_{50}$  of DDM was revealed at  $281.9\text{ }\mu\text{g/ml}$  and  $192.8\text{ }\mu\text{g/ml}$  for MCF-7 and MDA-MB-231 cells, respectively (Fig. 3a). The  $\text{IC}_{50}$  of AF was observed at  $180\text{ }\mu\text{g/ml}$  and  $184.1\text{ }\mu\text{g/ml}$  for MCF-7 and MDA-MB-231 cells, respectively (Fig. 3b).

### DDM<sup>Plus</sup>AF stability

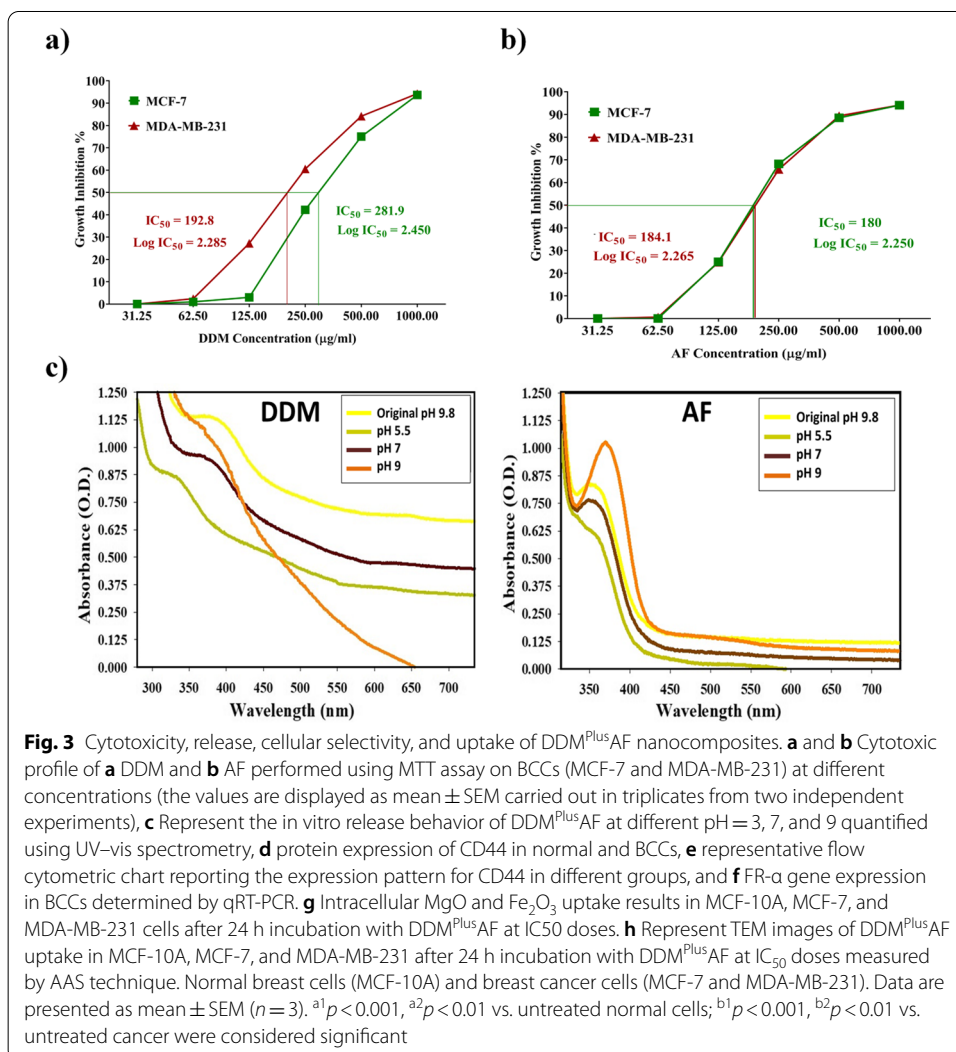
To determine nanoparticles stability, the sizes and charges of DDM and AF nanocomposites were monitored using dynamic light scattering (DLS) and zeta ( $\zeta$ ) potential analyses (as shown in Additional file 1: Data S1). Over 6 days dispersed in PBS plus 10% FBS, the average hydrodynamic diameter of DDM and AF remained essentially stable; nanoparticles did not aggregate. DLS measurements revealed that DDM and AF had a hydrodynamic diameter average of  $352.49\text{ nm}$ . Furthermore, as incubation time was increased, the  $\zeta$ -potential of nanoparticles was stabilized at values ranging from  $-0.01$  to  $-3.01\text{ mV}$  for DDM and AF. Negative surface charges on nanoparticles were neutralized by interactions with the medium's cationic constituents, resulting in lower negative-potential values. Notably, interactions did not result in nanoparticle aggregation even after a 6-day incubation period, indicating long-term hydrodynamic stability in a bio-relevant medium.

### DDM<sup>Plus</sup>AF release

The release behavior of DDM<sup>Plus</sup>AF in vitro was studied using UV-Vis at pH values of 5.5, 7, and 9 in phosphate buffer solutions (PBS) containing DMSO 0.1% and propylene glycol 0.1% to simulate the neutral environment of normal cells and acidic conditions in cancer cells to determine the pH-dependent drug-releasing properties. At pH 5.5, as shown in Fig. 3d, more than 55% of DDM<sup>Plus</sup>AF is released. However, due to protonation and solubility of DDM and AF in acidic environments, the release rate of DDM at pH 7 and 9 was less than 10% and 1% DDM, respectively, in 24 h, whereas less than 5% and 1% of AF were released over 24 h at pH 7 and 9, respectively.

### Cellular selectivity and uptake of DDM<sup>Plus</sup>AF

The expression levels of CD44 and FR- $\alpha$  were measured in normal breast cells and both cell lines of breast cancer to reveal the selectivity of DDM<sup>Plus</sup>AF (Fig. 3). In MCF-10A (normal cells) treated with DDM<sup>Plus</sup>AF, the data showed insignificant change in the levels of CD44 (Fig. 3d, e) and FR- $\alpha$  (Fig. 3f) as compared to untreated MCF-10A cells. When compared to MCF-10A, CD44 and FR- $\alpha$  expression levels were increased significantly in untreated MCF-7 (by 4.96- and 2.53-fold, respectively) and MDA (by 4.72- and 3.74-fold, respectively). However, when compared to untreated MCF-7 and MDA cells, there was a significant reduction in CD44 (Fig. 3d, e) and FR- $\alpha$  (Fig. 3f) expression in MCF-7 + DDM<sup>Plus</sup>AF (by 66.07 and 58.12%, respectively) and MDA + DDM<sup>Plus</sup>AF (by 67.37 and 72.76%, respectively). As a result of the HA and FA incorporation into the DDM<sup>Plus</sup>AF system, it is possible to conclude that DDM<sup>Plus</sup>AF is non-selective to normal cells and has a high affinity to CD44 and FR- $\alpha$  receptors that are over-expressed on breast cancer cell membranes.



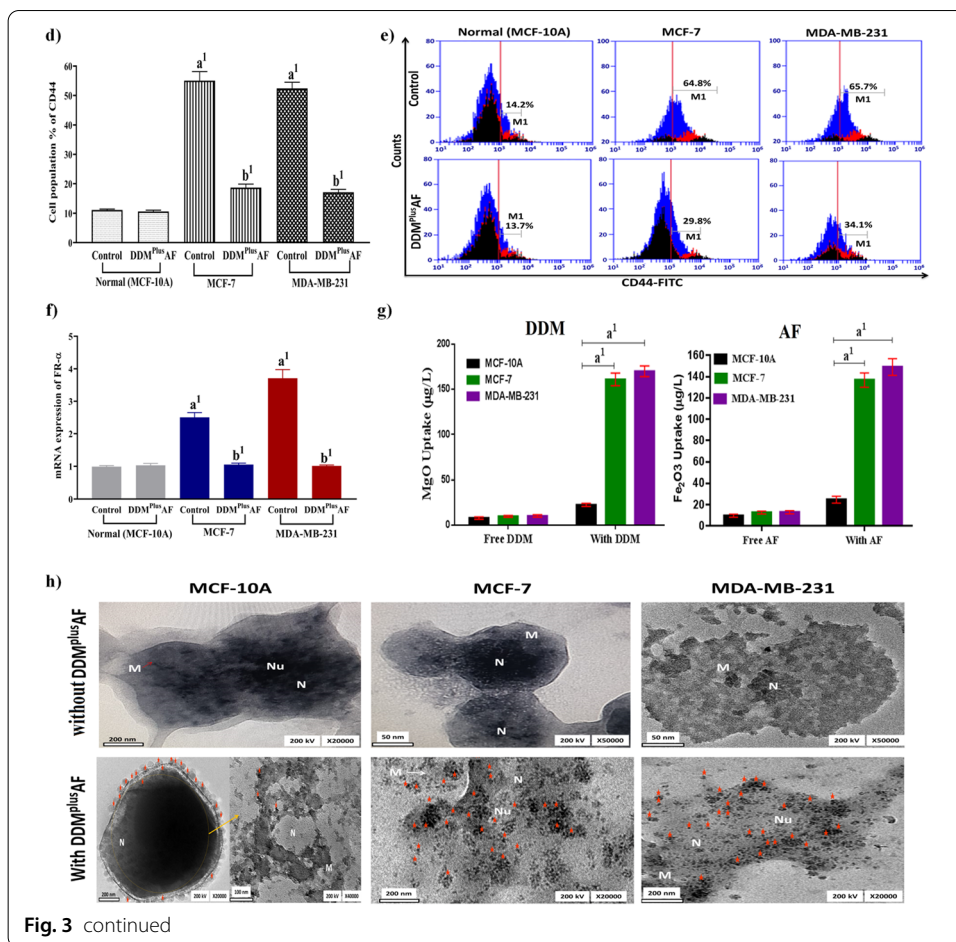
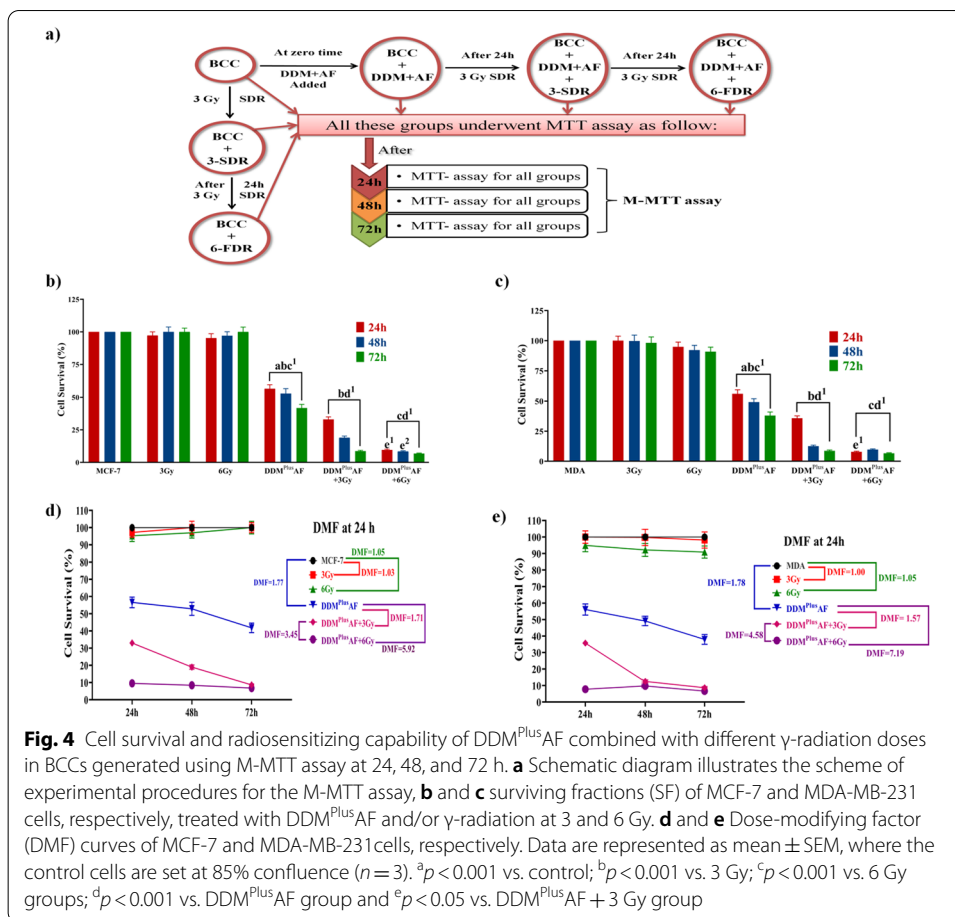


Fig. 3 continued

Figure 3g depicts the cellular uptake and localization of DDM<sup>plus</sup>AF in normal cells (MCF-10A) and cancer cells (MCF-7 and MDA-MB-231 cells) using AAS data. Quantitative data showed that DDM uptake was maximized by MCF-7 and MDA-MB-231 cells (7.2- and 7.6-fold, respectively) and AF was internalized by MCF-7 and MDA-MB-231 cells (5.5- and sixfold, respectively) over normal cells. These findings confirmed DDM<sup>plus</sup>AF's selective uptake into BCCs when compared to normal cells.

A TEM analysis was performed to visualize the internalized nanoparticles and assess their distribution in relation to subcellular compartments (Fig. 3h). In TEM images, abundant high electron density-staining nanoparticles were found inside the cells treated with DDM<sup>plus</sup>AF, which were not displayed in DDM<sup>plus</sup>AF untreated cells (Fig. 3h). The MCF-10A cells (normal) treated with DDM<sup>plus</sup>AF manifested a lower uptake of nanoparticles than the cancer cells (MCF-7 and MDA-MB-231 cells). In contrast, the uptake of nanoparticles by cancer cells treated with DDM<sup>plus</sup>AF was significantly higher, with a significant difference at  $p < 0.001$ . The uptake of DDM<sup>plus</sup>AF particles was calculated depending on the intracellular concentration of DDM<sup>plus</sup>AF. These values are measured against the estimated number of DDM<sup>plus</sup>AF introduced to the MCF-7 and MDA-MB-231 cells, which mean ~66.5 and 84.6% of nanoparticles, respectively, from IC<sub>50</sub> dose are more efficiently internalized than normal cells (Fig. 3h).



### Cell survival and radiosensitization of DDM<sup>Plus</sup>AF

To investigate the radiosensitizing ability of DDM<sup>Plus</sup>AF, multi-MTT assays were performed on both BCCs exposed to 3 Gy-SDR or 6 Gy-FDR as illustrated in Fig. 4a. In the current study, DDM<sup>Plus</sup>AF was selected as the synergistic therapy for cancer after it is significantly declined the cell viability of both BCCs, which was confirmed through the M-MTT assay carried out on DDM, AF and DDM<sup>Plus</sup>AF along with the both doses of  $\gamma$ -radiation (Additional file 1: Data S2a and b).

When cells were exposed to 3 Gy-SDR or 6 Gy-FDR, the data showed a non-significant change in survival rate between BCCs as compared to BCCs without therapy. However, DDM<sup>Plus</sup>AF therapy reduced the survival of MCF-7 cells by 43.46, 47.17, and 58.23% and by 43.94, 50.85 and 62.03% in MDA cells at 24, 48, and 72 h, respectively, compared to untreated BCCs (Fig. 4b, c).

On the other hand, compared to DDM<sup>Plus</sup>AF group, a significant elevation was observed in the survival of MCF-7 + 3 Gy treated cells by 1.84-, 1.89-, and 2.39-fold, MCF-7 + 6 Gy treated cells by 1.68-, 1.84-, and 2.39-fold, MDA + 3 Gy exposed cells by 1.78-, 2.03-, and 2.59-fold, and MDA + 6 Gy exposed cells by 1.69-, 1.87-, and 2.39-fold at 24, 48, and 72 h, respectively (Fig. 4b, c).

Furthermore, the BCCs survival rate was significantly decreased in MCF-7 + DDM<sup>Plus</sup>AF + 3 Gy group to 41.79, 64.11, and 79.40%, and in the

MDA + DDM<sup>Plus</sup>AF + 3 Gy group to 36.26, 74.52, and 77.07% at 24, 48, and 72 h, respectively, when compared to the DDM<sup>Plus</sup>AF group. Additionally, the DDM<sup>Plus</sup>AF + 6 Gy group induced a significant decrease in the survival fraction of MCF-7 to 83.11, 84.08, and 83.74%, and in MDA cells to 86.09, 80.16, and 82.44% at 24, 48, and 72 h, respectively, when compared to DDM<sup>Plus</sup>AF group (Fig. 4b, c).

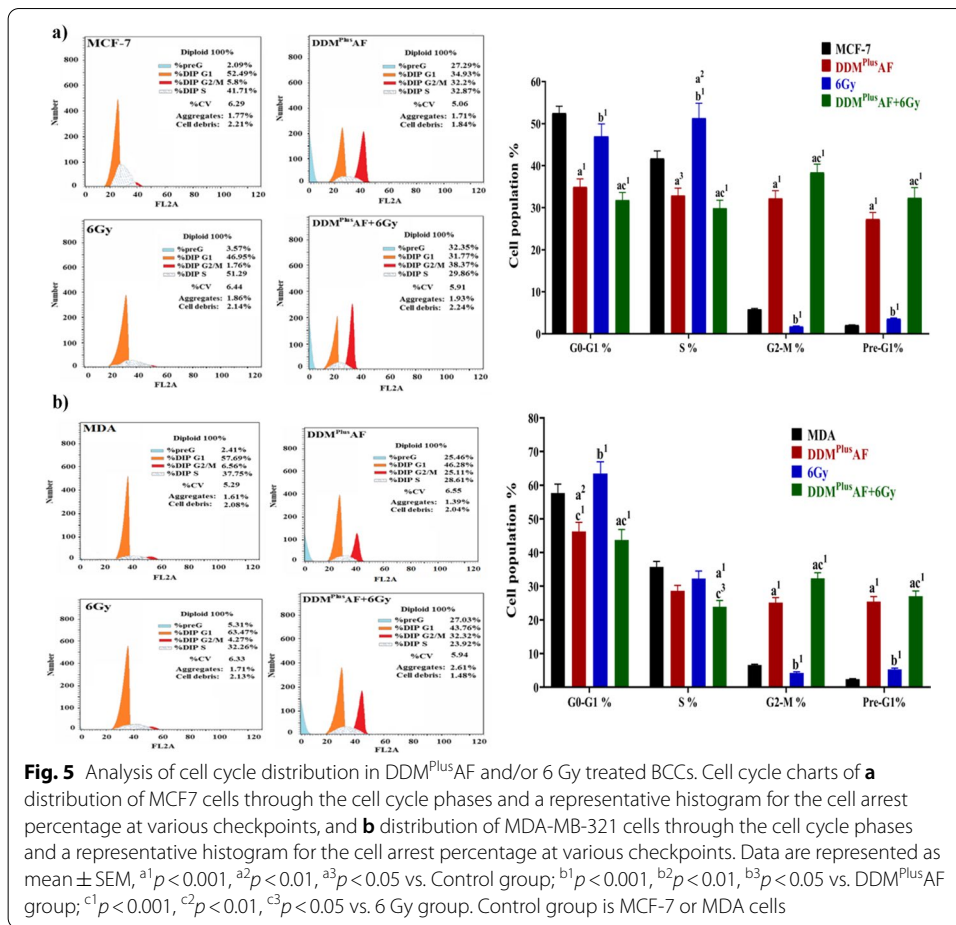
Moreover, the survival rate in the DDM<sup>Plus</sup>AF + 3 Gy group revealed a significant decline in MCF-7 cells to 66.10, 81.04, and 91.39%, and in MDA cells to 64.27, 87.45, and 91.13 compared to BCCs exposed to 3 Gy at 24, 48, and 72 h, respectively. In addition, when compared to BCCs exposed to 6 Gy at 24, 48, and 72 h, the growth inhibition rate in the DDM<sup>Plus</sup>AF + 6 Gy group was 89.97, 91.33, and 93.21% for MCF-7 cells and 91.79, 89.42, and 92.66% for MDA cells (Fig. 4a, b). Furthermore, when DDM<sup>Plus</sup>AF + 6 Gy was compared to DDM<sup>Plus</sup>AF + 3 Gy, MCF-7 cells survived at 71.01, 55.65, and 21.07%, respectively, while MDA cells survived at 78.19, 22.12, and 23.43% at 24 h, 48 h, and 72 h, respectively. According to the above survival data of all groups and time intervals, it was revealed that DDM<sup>Plus</sup>AF + 6 Gy after 24 h has the best anti-cancer effect (Fig. 4b, c).

Figure 4d, e) depicts the dose modifying factor (DMF) data for all groups, whereas, at 24 h, the dose–response rates of 3 Gy and 6 Gy were the same on BCCs. But after DDM<sup>Plus</sup>AF therapy, the dose–response rates of the DDM<sup>Plus</sup>AF + 3 Gy and DDM<sup>Plus</sup>AF + 6 Gy groups were elevated compared to each therapy alone. Furthermore, the DDM<sup>Plus</sup>AF + 6 Gy group had a higher dose–response rate than the DDM<sup>Plus</sup>AF + 3 Gy group. These results showed that DDM<sup>Plus</sup>AF induced a greater radiosensitizing modified effect with 6 Gy than with DDM<sup>Plus</sup>AF + 3 Gy; thus, the 6 Gy at 24 h was chosen for further investigations (Fig. 4d, e).

#### Cell cycle arrest and apoptosis analysis

Cell cycle distribution and cell apoptosis were measured using flow cytometry to assess DDM<sup>Plus</sup>AF's role as an anti-cancer and radiosensitizer to 6 Gy in BCCs. The cell cycle analysis of untreated BCCs (MCF-7 or MDA cells) showed an arrest at the G1 phase. When compared to MCF-7 cells, the MCF-7 + 6 Gy group displayed an arrest at the S phase (Fig. 5a), whereas the MDA + 6 Gy group showed a higher proportion in the G1 phase, comparable to MDA cells (Fig. 5b). Nevertheless, after DDM<sup>Plus</sup>AF therapy, a remarkable elevation in G2/M and pre-G1 phases was observed in both cell lines when compared to groups of BCCs and 6 Gy of each BCC. Furthermore, when compared to the untreated BCCs and BCCs exposed to 6 Gy of each cell line, the combination group DDM<sup>Plus</sup>AF + 6 Gy implied a higher proportion in G2/M and pre-G1 phases and a lower proportion in G1 and S phases in both cell lines.

The analysis of apoptotic cells revealed that the DDM<sup>Plus</sup>AF group had a higher percentage of apoptotic cells in both cell lines than the corresponding untreated BCCs (Fig. 6). Furthermore, when compared to the BCCs and BCCs + 6 Gy groups of each type, the combination group DDM<sup>Plus</sup>AF + 6 Gy has a higher percentage of apoptotic cells in both cell lines. Moreover, DDM<sup>Plus</sup>AF + 6 Gy induced an increase in necrotic cell percentage in both cell lines when compared to BCCs, 6 Gy, and DDM<sup>Plus</sup>AF of each BCC type.



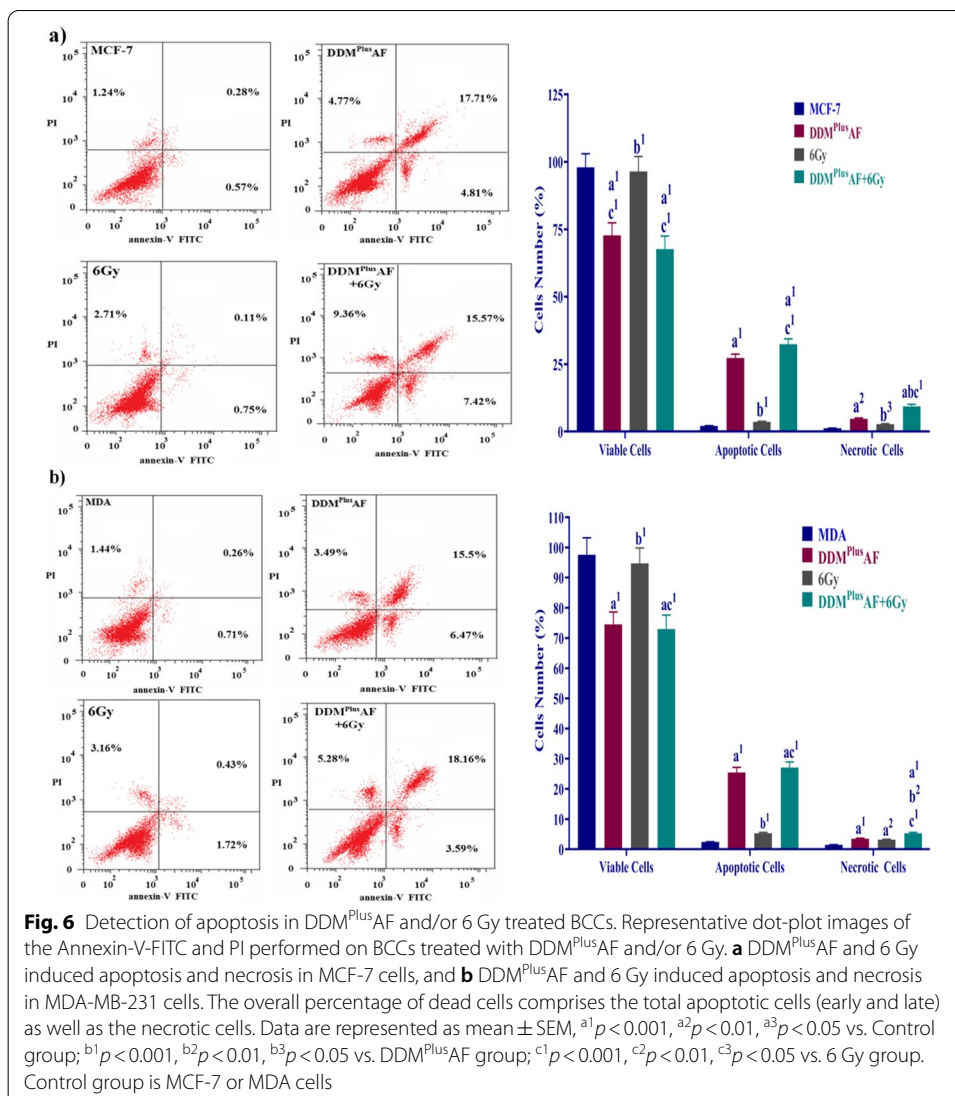
**Fig. 5** Analysis of cell cycle distribution in DDM<sup>Plus</sup>AF and/or 6 Gy treated BCCs. Cell cycle charts of **a** distribution of MCF7 cells through the cell cycle phases and a representative histogram for the cell arrest percentage at various checkpoints, and **b** distribution of MDA-MB-321 cells through the cell cycle phases and a representative histogram for the cell arrest percentage at various checkpoints. Data are represented as mean ± SEM, <sup>a1</sup>*p* < 0.001, <sup>a2</sup>*p* < 0.01, <sup>a3</sup>*p* < 0.05 vs. Control group; <sup>b1</sup>*p* < 0.001, <sup>b2</sup>*p* < 0.01, <sup>b3</sup>*p* < 0.05 vs. DDM<sup>Plus</sup>AF group; <sup>c1</sup>*p* < 0.001, <sup>c2</sup>*p* < 0.01, <sup>c3</sup>*p* < 0.05 vs. 6 Gy group. Control group is MCF-7 or MDA cells

### Modulatory effect of DDM<sup>Plus</sup>AF on tumor-promoting factors and metabolic reprogramming

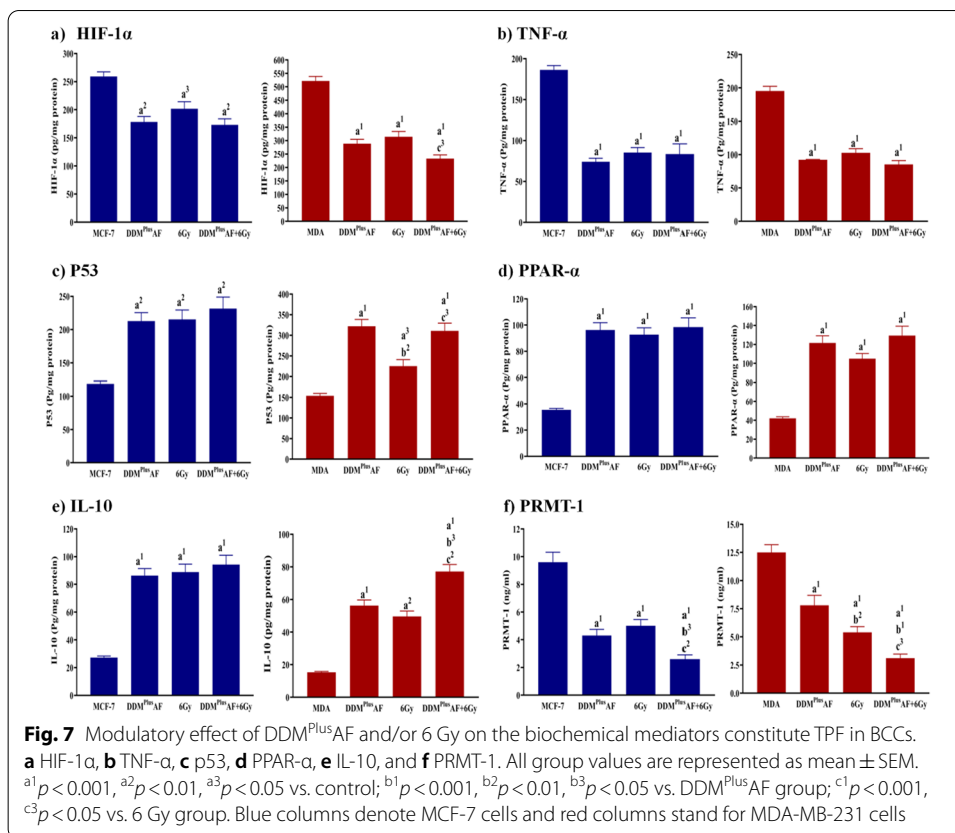
This study is designed to target the tumor-promoting factors (TPF) and metabolic reprogramming via the combination of DDM<sup>Plus</sup>AF with radiotherapy at 6 Gy in BC therapy. This was accomplished by evaluating the biochemical mediators constitute a tumor-promoting milieu (HIF-1α, TNF-α, IL-10, p53, PPAR-α, and PRMT-1) (Fig. 7) compared to the glycolytic metabolism (glucose, HK, PDH, lactate, and ATP) (Fig. 8) and signaling effectors (protein expression of AKT, AMPK, SIRT-1, TGF-β, PGC-1α, and gene expression of ERR-α) (Fig. 9).

#### Biochemical mediators constitute a tumor-promoting milieu

As demonstrated in Fig. 7, the DDM<sup>Plus</sup>AF group showed a significant reduction in the level of HIF-1α (31.18% for MCF-7 and 44.70% for MDA), TNF-α (60.20% for MCF-7 and 52.84% for MDA) (Fig. 7a, b), and PRMT-1 (55.21% for MCF-7 and 37.6% for MDA) (Fig. 7f), associated with a significant elevation in p53 (1.79-fold for MCF-7 and 2.09-fold for MDA), PPAR-α (2.71-fold for MCF-7 and 2.89-fold for MDA), and IL-10 (3.18-fold MCF-7 and 3.68-fold MDA) levels (Fig. 7c–e) when compared to the control BCCs. Exposure to 6 Gy induced a significant decrease in the levels of HIF-1α (22.19%



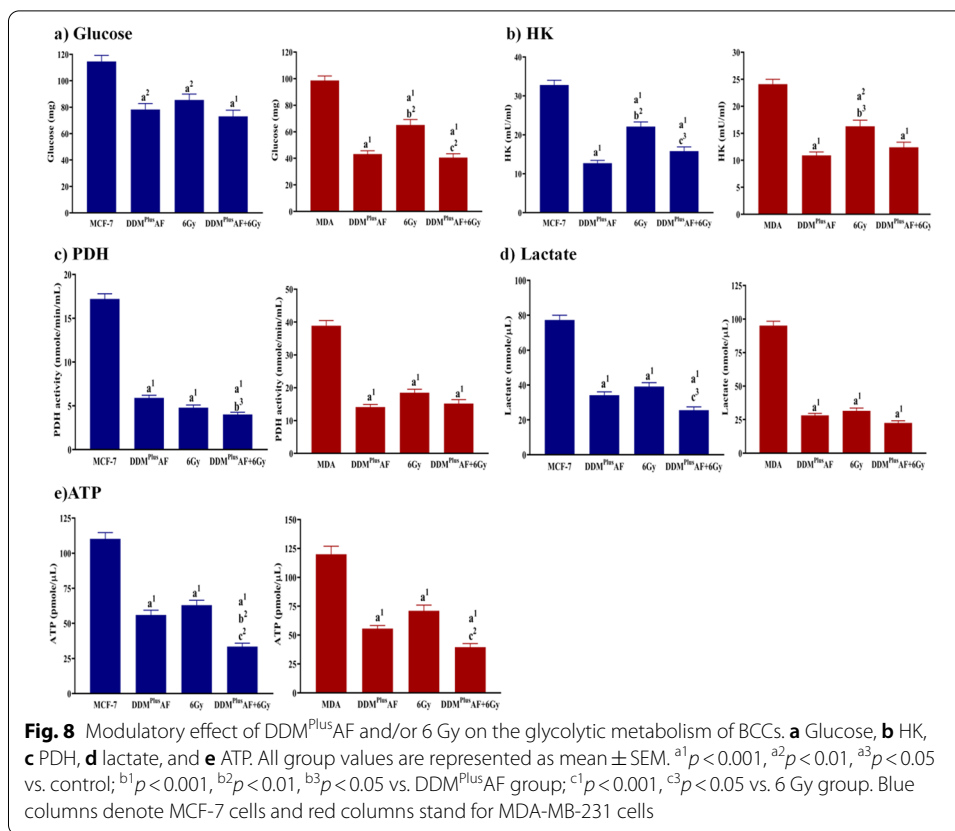
for MCF-7 and 39.79% for MDA) and TNF- $\alpha$  (54.19% for MCF-7 and 47.52% for MDA) (Fig. 7a, b) and PRMT-1 (47.81% for MCF-7 and 56.8% for MDA), associated with a significant increase of P53 (1.81-fold MCF-7 and 1.46-fold MDA), PPAR- $\alpha$  (2.61-fold for MCF-7 and 2.49-fold for MDA) and IL-10 (3.26-fold for MCF-7 and 3.24-fold for MDA) levels (Fig. 7c–e) when compared to the untreated BCCs. In DDM<sup>plus</sup>AF + 6 Gy group, the data display a significant diminish in the levels of HIF-1 $\alpha$  (33.15% for MCF-7 and 55.39% for MDA) and TNF- $\alpha$  (55.15% for MCF-7 and 56.37% for MDA) (Fig. 7a, b) and PRMT-1 (72.92% for MCF-7 and 75.2% for MDA), associated with a significant elevation of p53 (1.95-fold for MCF-7 and 2.02-fold for MDA), PPAR- $\alpha$  (2.77-fold for MCF-7 and 3.07-fold for MDA) and IL-10 (3.47-fold for MCF-7 and 5.04-fold for MDA) levels (Fig. 7c–e) when compared to BCCs without therapy. It was observed that the data of the MDA + DDM<sup>plus</sup>AF + 6 Gy group reveal a significant decrease in HIF-1 $\alpha$  (25.91%) (Fig. 7a), a considerable elevation in p53 (1.38-fold) (Fig. 7c) and IL-10 (1.56-fold) levels (Fig. 7e) as compared with the MDA + 6 Gy group; as well as markedly raised IL-10



level (1.37-fold) (Fig. 7e) when compared with the MDA + DDM<sup>Plus</sup>AF set. Conversely, the combination of DDM<sup>Plus</sup>AF and 6 Gy caused a significant diminish in PRMT-1 level in MCF-7 (39.53 and 48.10%, respectively) and MDA (60.26 and 42.59%, respectively) cells as compared with DDM<sup>Plus</sup>AF and 6 Gy groups, respectively, of the both cell lines (Fig. 7f).

### Glycolytic metabolism

In Fig. 8, the mediators of glycolytic pathway are discerned, when MCF-7 cells were treated with DDM<sup>Plus</sup>AF or 6 Gy, there was a significant diminution in glucose (31.67 and 25.39%) (Fig. 8a), HK (61.28 and 32.62%) (Fig. 8b), PDH (65.71 and 72.11%) (Fig. 8c), lactate (55.89 and 49.42%) (Fig. 8d), and ATP (49.18 and 42.81%) (Fig. 8e). In addition, when compared to the DDM<sup>Plus</sup>AF group, 6 Gy treated BCCs showed a significant increase in HK (1.74-fold) in both cell lines. While, the results of DDM<sup>Plus</sup>AF + 6 Gy manifested a significant reduction in the levels of glucose (36.67%) as compared with MCF-7 group, HK (51.83 and 28.51%), lactate (66.88 and 34.53%) as compared to MCF-7 and 6 Gy groups, respectively, and PDH (76.70 and 32.05%) as compared with MCF-7 and DDM<sup>Plus</sup>AF groups, respectively, as well as ATP (69.60, 40.18, and 46.84%) as compared to MCF-7, DDM<sup>Plus</sup>AF, and 6 Gy groups, respectively. In MDA cell line, the data of DDM<sup>Plus</sup>AF or 6 Gy groups detected a significant decrease in glucose (56.19 and 33.97%) (Fig. 8a), HK (54.77 and 32.41%) (Fig. 8b), PDH (63.75 and 52.44%) (Fig. 8c), lactate (70.45 and 66.77%) (Fig. 8d), and ATP (53.69 and 40.85%) levels (Fig. 8e), respectively,

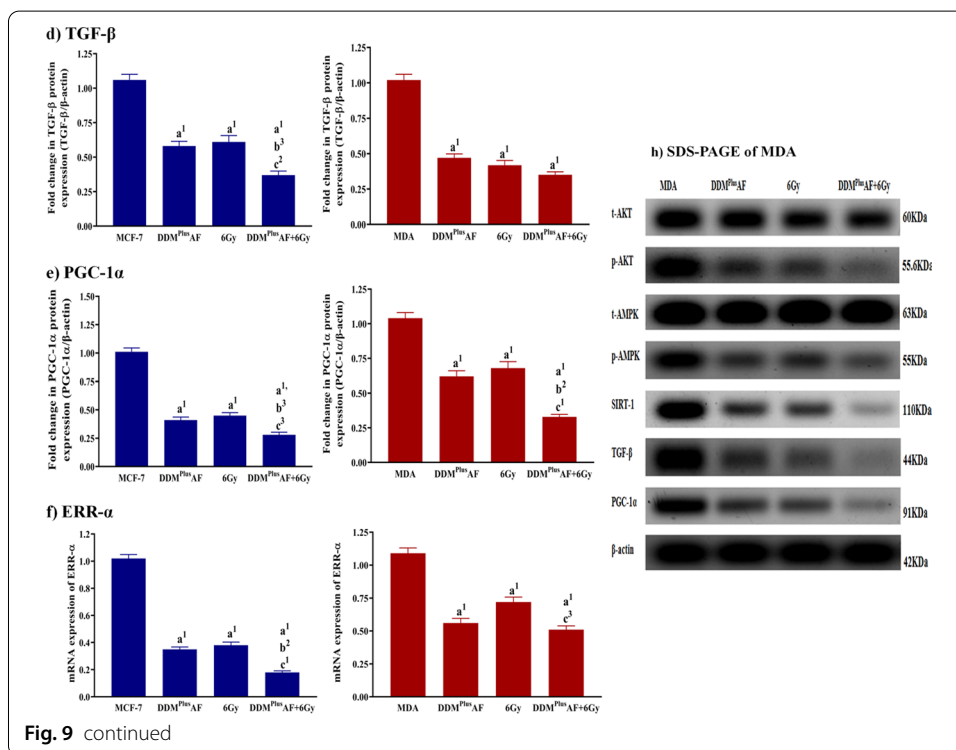
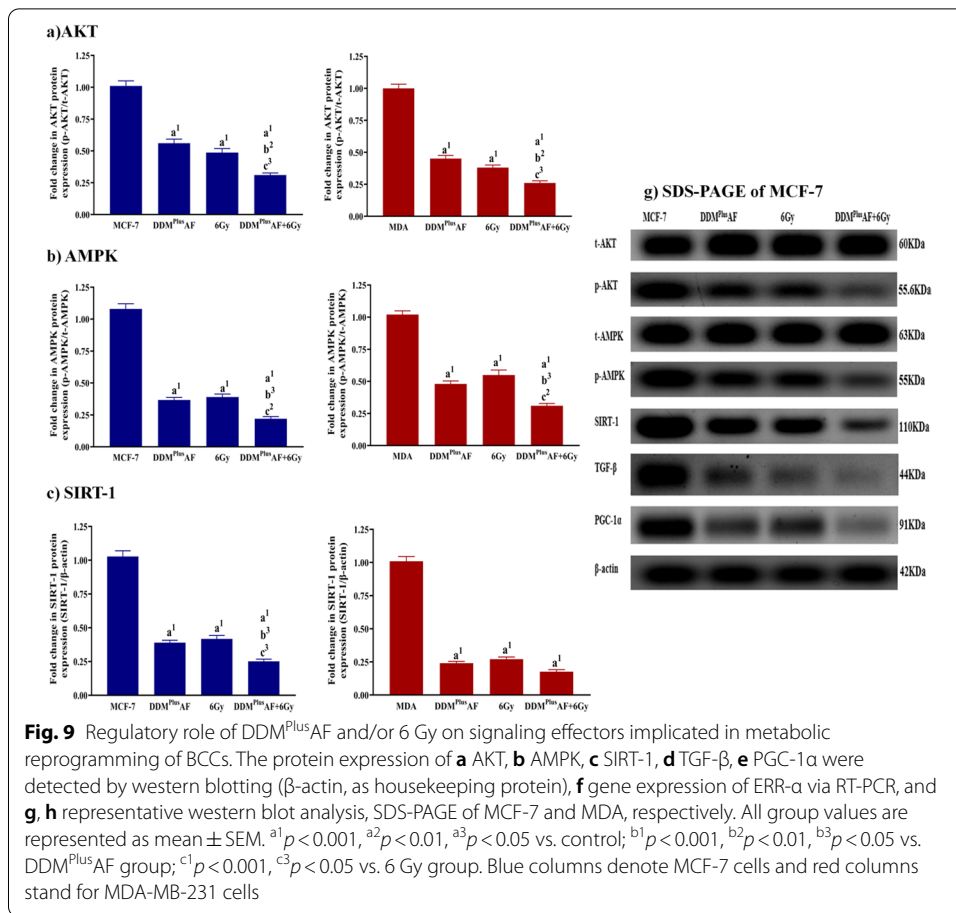


as compared to the untreated MDA cells. Moreover, when compared to the DDM<sup>Plus</sup>AF group, 6 Gy showed a significant increment in glucose (1.51-fold) and HK (1.49-fold) levels. When compared to MDA and 6 Gy groups, the combination group of DDM<sup>Plus</sup>AF and 6 Gy showed a significant decrement in glucose (58.92 and 37.79%), ATP (67.86 and 44.25%); and in HK (48.55%), PDH (60.92%), and lactate (76.34%) levels, when compared to the MDA group set (Fig. 8).

### Signaling effectors implicated in oncogenesis and metabolic reprogramming of BCCs

The data illustrated in Fig. 9a–f revealed a profound down-regulation in the protein expression of MCF-7 AKT by 44.55 and 51.81% (Fig. 9a), AMPK by 66.05 and 63.89% (Fig. 9b), SIRT-1 by 62.02 and 61.03% (Fig. 9c), TGF-β by 45.28 and 42.45% (Fig. 9d), and PGC-1α by 55.44 and 59.43% (Fig. 9e) paralleled by a substantial decline in the gene expression of ERR-α by 65.69 and 62.74% (Fig. 9f), respectively, in DDM<sup>Plus</sup>AF and 6 Gy groups, respectively, when compared to the untreated MCF-7 group. Similarly, a pronounced curtailment in the protein expression of AKT by 55 and 62%, AMPK by 52.94 and 46.20%, SIRT-1 by 76.24 and 73.28%, TGF-β by 53.92 and 58.99%, and PGC-1α by 40.38 and 34.61% coupled with a significantly lowered gene expression of ERR-α by 48.62 and 33.94% in DDM<sup>Plus</sup>AF and 6 Gy groups as compared to the control MDA group (Fig. 9a–f).

In DDM<sup>Plus</sup>AF + 6 Gy of MCF-7 treated cells, the results showed a significant reduction in the protein expression of AKT by 69.30, 44.64, and 36.30%, AMPK by 79.63, 40.00,



and 43.59%, SIRT-1 by 75.66, 35.89, and 40.00%, TGF- $\beta$  by 65.09, 36.21, and 39.34%, and PGC-1 $\alpha$  by 72.28, 37.78, and 31.66%, as well as the gene expression of ERR- $\alpha$  by 82.35, 48.57, and 52.63%, respectively, when compared to MCF-7, DDM<sup>Plus</sup>AF, and 6 Gy groups, respectively (Fig. 9a–f). Additionally, when compared to MDA, DDM<sup>Plus</sup>AF, and 6 Gy groups, the MDA + DDM<sup>Plus</sup>AF + 6 Gy group displayed a significant diminution in the protein expression of AKT by 74.00, 42.21, and 31.58%, AMPK by 69.61, 35.42, and 43.50%, and PGC-1 $\alpha$  by 68.36, 64.93, and 51.62%, respectively (Fig. 9). Moreover, as compared with MDA group, the protein expression of SIRT-1 and TGF- $\beta$  were markedly lowered by 82.50 and 65.69%, respectively, while the gene expression of ERR- $\alpha$  revealed a significant decline by 35.24 and 29.21%, when compared to MDA and 6 Gy groups, respectively (Fig. 9a–f).

## Discussion

The CD44 and FR- $\alpha$  expression data revealed that the selectivity-mediated cellular uptake of DDM<sup>Plus</sup>AF nanocomposites was reduced in normal breast cells (MCF-10A) and maximized in BCCs. Our data revealed that the incorporation of surface annex receptor-mediated uptake (HA and FA), which enabled the optimum tumor targeting, augmented the selective cytotoxicity of DDM<sup>Plus</sup>AF towards BCCs with no affinity for normal breast cells. This uptake indicates HA/FA-mediated endocytosis by BCCs. Therefore, DDM and AF can enter cancer cells through binding to a specific receptors CD44 and FR- $\alpha$ , which are over-expressed on BCCs via HA/FA, respectively (Liu et al. 2019). The results of pH-responsive release of DDM<sup>Plus</sup>AF were shown to be performed in acidic conditions (pH = 5.5) of cancer rather than normal cells, and this result supported with the data reported by Guo et al. (2017) and Jurczyk et al. (2021).

Radiotherapy has been harnessed for over a century to treat patients with cancer, largely based on the rationale that rapidly proliferating cancer cells are more sensitive than normal cells for the DNA damage response, but in terms of the consequences of radiation-induced tumor cell death and various signaling pathways involved in sensitivity, resistance, and further molecular sensors that modify the tumor response to radiation (Baskar et al. 2014). Furthermore, it was found that the alterations in the glycolytic metabolism were shown to contribute to the declining radiotherapy effect. Additionally, radiotherapy effects primarily depend on glucose metabolism, while the mitochondrial metabolic alterations can be involved in this process as well (Tang et al. 2018). Therefore, targeting of the metabolic enzymes, such as glucose transporters, HK, pyruvate kinase M2, lactate dehydrogenase A, PDK, fatty acid synthase, and glutaminase, can enhance the efficacy of chemotherapy or radiotherapy, as observed, for example with 2-DG and DCA when combined with chemotherapy or radiotherapy (Zhao et al. 2013).

The anti-cancer effect of DDM<sup>Plus</sup>AF with  $\gamma$ -radiation was demonstrated by the reduction of both BCCs' viability through cell cycle arrest at G2/M and pre-G1 phases, which generates apoptotic cell death compared to untreated cancer cell lines. Additionally, this could be attributed to their modulatory effects that are displayed on TME-associated TPF and mediators, glycolytic pathways, and signaling molecules as revealed in the current study. Noteworthy, the innovative DDM and AF core-shell nanocomposites have numerous attractive characteristics. DDM core-shell induced an anti-cancer effect through its components such as the ability of 2-DG, a stable glucose analogue, to

inhibit glycolysis due to the formation and intracellular accumulation of 2-deoxy-D-glucose-6-phosphate (2-DG6P), inhibiting the function of HK and glucose-6-phosphate isomerase, and inducing apoptotic cell death (Pajak et al. 2019). Moreover, DCA reverses the Warburg effect in human tumor cells by inhibiting PDK, re-activating PDH and OXPHOS, as well as decreasing pyruvate and lactate levels, leading to decreased expression of HIF-1 $\alpha$ . As a consequence of OXPHOS stimulation, DCA increases reactive oxygen species (ROS) production by the mitochondrial respiratory chain and induces other downstream changes in mitochondrial function, resulting in tumor cell-selective apoptosis, decreased cancer cell proliferation, and increased host survival (James et al. 2017). Furthermore, AF core-shell induced an anti-cancer effect via amygdalin, which inhibits TNF- $\alpha$  levels, AKT-mTOR, and TGF- $\beta$  pathways, while increasing the levels of P53, Bax, cytochrome c, caspase-3, and finally cell cycle arrest at G2/M (Liczbiński and Bukowska 2018; El-Desouky et al. 2020). This inhibitory effect of AF on TNF- $\alpha$  could explain why aerobic glycolysis and ATP production in BCCs are declining. In support of this notion, the study of Vaughan et al. (2013) reported that curcumin, as anti-inflammatory agent, suppresses TNF- $\alpha$  and, as a result, reduces aerobic glycolysis and ATP production in MCF-7 cells. Furthermore, Liu et al. (2016) elucidated that inhibiting HIF-1 $\alpha$  and TNF- $\alpha$  prevents metabolic reprogramming in cell models of dextran sulfate sodium (DSS)-induced colitis in mice, which is used to treat this disease. Moreover, the studies of Ahamed et al. (2013) and Behzadi et al. (2019) demonstrated that MgO and Fe<sub>2</sub>O<sub>3</sub> nanoparticles induce apoptosis in cancer cells through increasing the load of intracellular ROS. This elevation induced an up-regulation of p53 level in cancer cells (Ahamed et al. 2013; Perillo et al. 2020). In addition, it was found that the p53 protein induces a decrease in glycolytic pathway, and overall levels of intracellular ROS (Puzio-Kuter 2011).

Moreover, to maintain cancer cell proliferation and survival in the hypoxic microenvironment, an interplay between HIF-1 and a variety of oncogenes such as p53, AMPK, and AKT signaling pathways has been observed to contribute to the metabolic reprogramming of cancer cells and to control mitochondrial electron transport chain functioning and energy production (Moldogazieva et al. 2020). Additionally, it was found that hypoxia up-regulates PRMT-1 (Wrzesinski and Fey 2018). On the other hand, Lee and Park (2011) demonstrated that reduction of HIF-1 $\alpha$  accompanied by decreased AMPK activity. Furthermore, it was demonstrated that p53 up-regulation decreased the stability of PGC-1 $\alpha$  via the ubiquitin proteasome pathway, which was mediated by AKT inhibition and glycogen synthase kinase (GSK-3 $\beta$ ) activation (Deng et al. 2020). Moreover, increasing p53 activity could reduce the expression level of SIRT-1 through a negative feedback loop (Deng 2009). According to Tan et al. (2016), the down-regulation of AMPK and SIRT-1 signaling molecules led to the suppression of PGC-1 $\alpha$ . As a result, the PGC-1 $\alpha$ /ERR- $\alpha$  axis and its downstream promote glycolysis and OXPHOS in cancer (Tan et al. 2016) were inhibited, as revealed in our data. The elevation of PPAR- $\alpha$  level observed in this study could be attributed to 2DG, which mimics the dissociative effect of glucose-6-phosphate on the HK/VDAC (voltage-dependent anion channel) complex (Vamecq et al. 2012); Whereas, it was found that the activation of PPAR- $\alpha$  was attributed to HK and VDAC dissociation when fenofibrate, a PPAR- $\alpha$  agonist, was administered to cell lines and a mouse model of oral cancer (Antonosante et al. 2018). PPAR- $\alpha$

activation has anti-cancer effects as a possible trigger of ineffective tumor metabolism, blocking fatty acid synthase (FAS) pathway, which is one of cancer cells metabolic peculiarities along with aerobic glycolysis, inhibiting AKT phosphorylation, and imparting an anti-inflammatory properties (Grabacka and Reiss 2008; Antonosante et al. 2018). This anti-inflammatory effect of PPAR- $\alpha$  activation is related to an elevation of IL-10 and a reduction in TNF- $\alpha$  expression (Cao et al. 2014). Most importantly, it was found that the increase of IL-10 inhibits glucose uptake and glycolytic flux by regulating the glycolytic enzymes (Ip et al. 2017).

## Conclusions

DDM<sup>Plus</sup>AF is a combinatorial targeted anti-cancer platform with multifunctional effects that induces cell cycle arrest at G2/M and pre-G1 phases and generates apoptotic cell death in both BCC lines. Its constituents, which include 2DG (hexokinase inhibitor), DCA (PDK inhibitor), and amygdalin, suppress the aerobic glycolytic pathway and modulate TPF mediators and signaling effectors, are responsible for this effect. Specifically, through a significant decrease in glucose, HK, PDH, lactate, and ATP, concurrent with a significant reduction in protein expression of AKT, AMPK, SIRT-1, TGF- $\beta$ , and PGC-1 $\alpha$ , as well as the gene expression of ERR- $\alpha$ . Moreover, a significant reduction in HIF-1 $\alpha$ , TNF- $\alpha$  and PRMT-1 was associated with a significant elevation in IL-10, P53, and PPAR- $\alpha$  (Fig. 10). Interestingly, the DDM<sup>Plus</sup>AF augmented the radiosensitivity of MCF-7 and MDA-MB-231 cell lines. Collectively, these effects of DDM<sup>Plus</sup>AF in combination with radiotherapy support its potential implication in theranostic applications for breast cancer therapy.

## Materials and methods

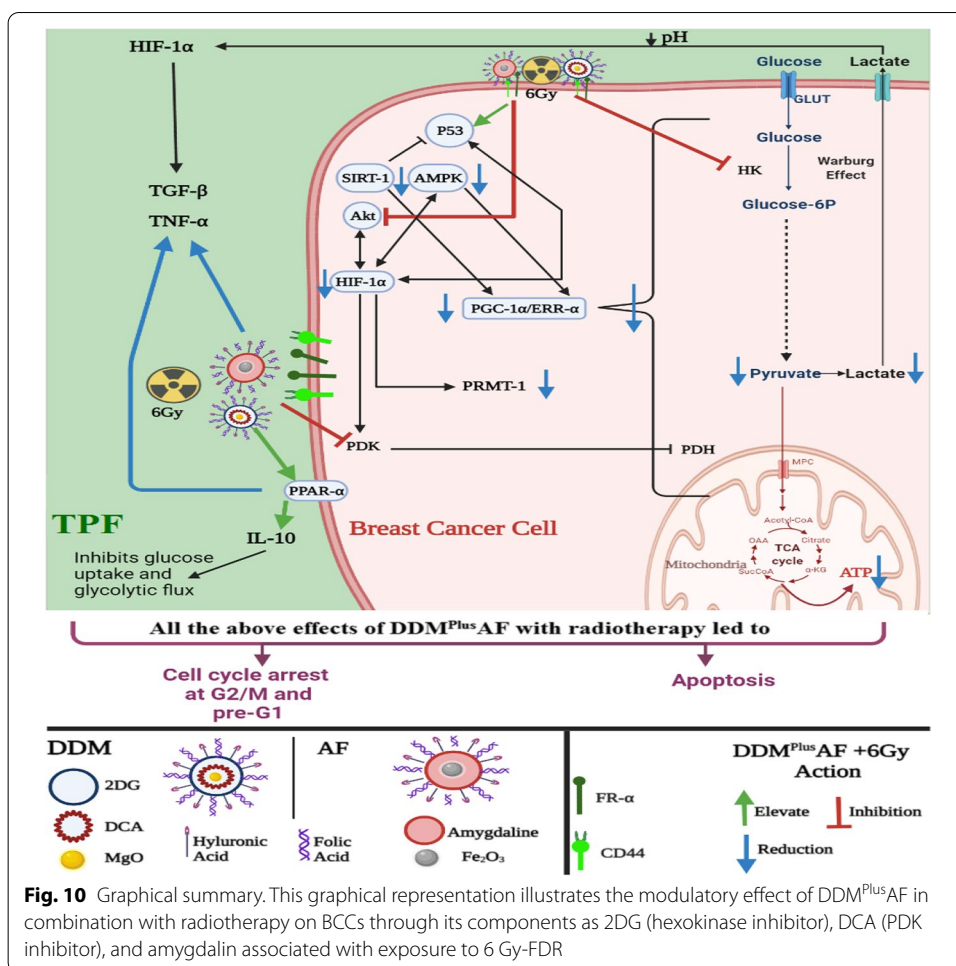
### Synthesis of DDM

#### *Step one: preparation of MgO nanoparticles*

MgO nanoparticles (MgO-NPs) were synthesized following the technique mentioned by Diana et al. (2021) with slight modifications. Briefly, urea was dissolved into an aqueous solution of magnesium nitrate (0.25 M) under continuous stirring at 75 °C until gel creation. After that, MgO-NPs were synthesized by placing the gel at 600 °C in a muffle furnace for 3.5 h. Finally, the prepared MgO-NPs were rinsed with de-ionized water (D.I.W) and dehydrated at 75 °C for 3 h, as shown in Additional file 1: Data S3a-1.

#### *Step two: preparation of 2DG@DCA@MgO*

This unique composite construction was developed by a manageable impregnation process. After conducting water bath sonication for 60 min, the prepared MgO-NPs from step one were dispersed in 100 ml ethanol. The aqueous solutions of previously prepared DCA and 2DG (10 mM) were then added to the dispersion after 3 h of continuous stirring at room temperature (24 °C). As shown in Additional file 1: Data S3a-2, the developed particles were settled, collected, cleaned, and dehydrated.



**Step three: incorporation of 2DG@DCA@MgO with HA and FA**

The prepared nanocomposite structure from step two was dispersed in D.I.W for 40 min using water bath sonication. The solution was then mixed with 20 mM aqueous solutions of HA and FA, which were then sonicated for 45 min. The mixture was then stirred continuously for 3 h. Finally, the powder was obtained using centrifugation and dehydrated at 85 °C for 2 h (see in Additional file 1: Data S3a-3).

**Synthesis of AF**

**Step one: preparation of Fe<sub>2</sub>O<sub>3</sub> nanoparticles**

Fe<sub>2</sub>O<sub>3</sub> NPs were prepared according to the method described by Sankadiya et al. (2016) with minor modification. Firstly, 5.40 g of FeCl<sub>3</sub> · 6H<sub>2</sub>O was dissolved in (100 ml) D.I.W. using magnetic stirrer at ambient temperature for 15 min. Then, drop-by-drop, NH<sub>4</sub> OH solution (15%) was added into the above-mentioned solution to make reaction pH=8. The reaction was then stirred for 2 h at ambient temperature in the stirrer. The precipitate was then collected using a high-speed centrifuge running at 5000 rpm for 20 min. The formed precipitate was then washed several times using D.I.W. The purified precipitate was then dried in vacuum oven at 80 °C for 8 h.

Finally, the dried powder was then annealed at 200 °C for 3 h as shown in Additional file 1: Data S3b-1.

#### **Step two: preparation of Amygdaline@Fe<sub>2</sub>O<sub>3</sub> and its incorporation with HA and FA**

The synthesized Fe<sub>2</sub>O<sub>3</sub> NPs (250 mg) prepared from step one were dispersed in 100 ml D.I.W. using sonication for 30 min. Amygdaline (B 17) was then poured into the above dispersion under constant stirring at room temperature. Following that, FA-HA (250 mg) was added into the above mixture under constant stirring for 2 h. The prepared powder was then collected, washed with D.I.W., and dried at 80 °C for 2 h as presented in the Additional file 1: Data S3b-2.

#### **Characterization of DDM and AF**

Firstly, the stoichiometry of the synthesized nanocomposite samples is examined by employing the energy-dispersive X-ray spectra (EDX) (JEOL JSM-5600 LV, Japan). To confirm the formation of the exact sample with detected functional groups, Fourier transform infrared (FTIR) spectroscopy (NICOLET iS10 model instrument) is conducted over a wide range (400–4000 cm<sup>-1</sup>). The crystal structure of the nanocomposite samples was investigated using X-ray diffraction technique (XRD; Shimadzu XRD-6000). XRD patterns are obtained in the range of 2θ from 17° to 90° at room temperature. Cu Kα is used as a radiation source with a wavelength λ = 0.15408 nm, a scan rate of 0.8°/min, an operation voltage of 50 kV, and a current of 40 mA (Belavi et al. 2012; Reheem et al. 2016). Information on the surface morphology of the nanocomposite samples' particles is obtained using scanning electron microscopy (SEM) (JEOL JSM-5600 LV, Japan). Finally, the shape and size of the synthesized nanocomposite samples were obtained by high resolution transmission electron microscopy (HR-TEM) (JEOL JSM-5600 LV, Japan).

#### **Stability of DDM and AF**

To determine the stability of both nanocomposites DDM and AF, the charges and sizes were measured through the incubation of DDM<sup>Plus</sup>AF with phosphate buffer solutions (PBS) and 10% fetal bovine serum (FBS; pH 7.4) at body temperature (37 °C) using dynamic light scattering (DLS) and determining zeta (ζ) potential over 6 days (Angelopoulou et al. 2019).

#### **Cell lines and cell culture**

The breast cell lines used in this investigation were purchased from the Cell Culture Department, VACSERA (Cairo, Egypt). Normal human breast cells (MCF-10A), as well as human MCF-7 (luminal A) and MDA-MB-231 (Triple negative B) BCCs, were cultured in DMEM (Dulbecco's Modified Eagle Medium) supplemented with penicillin (100 U/ml), streptomycin (100 mg/ml), and 10% FBS (fetal bovine serum) in a 5% CO<sub>2</sub> humidified chamber at 37 °C.

### Cytotoxicity assay

MTT (3-(4,5-dimethylthiazol-2yl)-2,5-diphenyltetrazolium bromide) (Sigma-Aldrich, USA) assay on both MCF-7 and MDA-MB-231 cell lines was used to investigate the cytotoxic effect of DDM and AF, as described by Van de Loosdrecht et al. (1994). DDM and AF were dissolved in dimethyl sulfoxide (DMSO) and propylene glycol (Sigma-Aldrich, USA), respectively. The stocks were then diluted with a culture medium to the indicated concentration for treatment before usage, and the final concentration of DMSO and propylene glycol in each well was 0.1% (V/V). Cells that were treated with the vehicle only, were kept as the control group. Briefly, in the 96-well tissue culture plate, cells were inoculated with  $1 \times 10^5$  cells/ml (100  $\mu$ l/well) and incubated at 37 °C for 24 h to develop a complete monolayer sheet. The growth medium was decanted from 96-well plates after a confluent sheet of cells was formed; the cell monolayer was washed twice with wash media. Twofold dilutions to both DDM and AF were made in RPMI medium with 2% serum (maintenance medium). Then, 0.1 ml of each dilution was tested in different wells leaving 3 wells as control, receiving only maintenance medium. The plate was incubated at 37 °C and examined. Cells were checked for any physical signs of toxicity, e.g., partial or complete loss of the monolayer, rounding, shrinkage, or cell granulation. A MTT solution was prepared (5 mg/ml in PBS), and after that, 20  $\mu$ l of MTT solution was added to each well. Place on a shaking table at 150 rpm for 5 min to thoroughly mix the MTT into the medium. Incubate (37 °C, 5% CO<sub>2</sub>) for 1–5 h to allow the MTT to be metabolized. Dump off the media and then resuspend formazan (MTT metabolic product) in 200  $\mu$ l of DMSO. Place on a shaking table at 150 rpm for 5 min to thoroughly mix the formazan into the solvent. Read optical density at 560 nm and subtract background at 620 nm. Optical densities should be directly correlated with cell quantities. Then, the half-maximal inhibitory concentration (IC<sub>50</sub>) was calculated. The cell morphology was recorded using a light inverted microscope fitted with a digital camera (Nikon, Japan). We performed all experiments in triplicate.

### Release of DDM and AF in vitro

To investigate the release of DDM and AF, suspensions of each were exposed at 37 °C conditions to pH 5.5, 7, and 9. The particles were collected at predetermined time intervals using an external magnet (1.3 Tesla), and the supernatant was saved for examination after 24 h of incubation. The released proportions of MgO and Fe<sub>2</sub>O<sub>3</sub> were quantified using UV–Vis at absorbance of 487 nm and 562 nm, respectively.

### Cellular selectivity and uptake of DDM<sup>Plus</sup>AF

Normal breast cells (MCF-10A) and BCCs (MCF-7 and MDA-MB-231) were seeded in 24-well plates with round coverslips at a density of  $2 \times 10^4$  cells/well. The next day, cells were incubated with medium containing an IC<sub>50</sub> dose of DDM and an IC<sub>50</sub> dose of AF. After 24 h incubation, the cells were washed three times with PBS and divided into four parts to perform four methods. The first and second methods were used to investigate the cellular selectivity of DDM<sup>Plus</sup>AF, which was accomplished by measuring CD44 expression by flow cytometric analysis using an FITC-conjugated anti-CD44 (1:400, Cat.

No# YKIX337.8, eBioscience) incubated with cells for 30 min at 4 °C, and measuring of FR- $\alpha$  expression by qRT-PCR as described in real-time PCR part.

The third and fourth methods were performed to investigate cellular uptake of DDM<sup>Plus</sup>AF, which was done by estimating MgO and Fe<sub>2</sub>O<sub>3</sub> concentration in normal and cancer cells by an atomic absorption spectrophotometer (AAS) and imaging of DDM<sup>Plus</sup>AF in normal and cancer cells using transmission electron microscopy (TEM), respectively.

The AAS model (AI-1200) was used with an air-acetylene burner (slot length, 11 cm). Instrumental settings were as follows: Wavelength [MgO=285.2 nm, Fe<sub>2</sub>O<sub>3</sub>=248.3 (Najim 2017)], lamp current (5 mA), slit width (0.2 nm), air-flow (1.8 L/min), ignition-flow (2.4 L/min). A standard solution of MgO and Fe<sub>2</sub>O<sub>3</sub> was prepared immediately by serial dilution of a 1000 mg/L stock solution (Scharlau Chemie) with de-ionized water prior to use. After 24 h incubation, the cells were washed three times with PBS, then centrifugation was carried out at 3000 rpm for 5 min and the supernatant was aspirated by using Pasteur pipette into another plain bottle. Supernatant and pellet cell samples were diluted with de-ionized water and homogenized before determination of MgO and Fe<sub>2</sub>O<sub>3</sub> concentrations (Planeta et al. 2021).

In brief, the imaging of DDM<sup>Plus</sup>AF by TEM was performed via fixation of cells in 2.5% glutaraldehyde, at 0.1 M Phosphate Buffer, pH 7.4 (Electron Microscopy Sciences, Hatfield, PA) for 1 h at room temperature. Cells were then scraped off the plates, centrifuged at a low speed, and suspended in 2.5% glutaraldehyde. Samples were further processed at the Egyptian atomic energy authority by post-fixation in 1% osmium tetroxide, rinsing in distilled water, and dehydration through a graded series of acetone. At the end, samples were embedded in epoxy resin and cut into 70 nm sections that were then analyzed and photographed by JEOL 100CXII electron microscope (Janic et al. 2018).

### **Irradiation**

All the irradiated groups of MCF-7 and MDA-MB-231 culture cell lines were irradiated at 85% confluence with a Canadian gamma cell-40, (<sup>137</sup>Cs) at the NCRRT (Cairo, Egypt) as fractionated doses, each of 3 Gy with a dose rate of 0.012 Gy/s. The dosimetry was used for all the experiments to ensure uniformity of dose and dose rate delivered using a Fricke reference standard dosimeter ISO/ASTM E 51026 (2015).

### **Multi-MTT assay**

A multiple-MTT (M-MTT) assay was performed to measure the BCCs radiosensitivity of nano-core-shell composites DDM<sup>Plus</sup>AF at 3 Gy (single dose radiotherapy; SDR) and 6 Gy (fractionated dose radiotherapy; FDR) after 24, 48, and 72 h from exposure to  $\gamma$ -rays according to the method of Buch et al. (2012) as illustrated in Fig. 4a. Briefly, the cells incubated in 96-well plates for 24 h ( $2 \times 10^3$  cells per well) before being supplemented with 100  $\mu$ l of MTT (3-(4,5-dimethylthiazol-2-yl)-2, 5-diphenyltetrazolium bromide) reagent (5 mg/ml in PBS, 20  $\mu$ l/well) to each well and incubated for 30 min at 37 °C. Thereafter, MTT solution was removed. After the addition of 180  $\mu$ l of DMSO the plates were incubated for 15 min at 37 °C to dissolve the formazan crystals. Eventually, the absorbance of each well was measured at 570 nm using an ELISA plate reader (BioTeck, Bad Friedrichshall, Germany). Following the conduction of proliferation/

inhibition assays, the survival curves were calculated and utilized to obtain the Dose-Modifying Factor (DMF) calculated at the iso-effect of survival fraction (SF) = 50% with radiation treatment alone respect to combined treatments (Minafra et al. 2019).

### Cell culture models

In the current study, the cultures of each MCF-7 and MDA-MB-231 cell lines were divided into four groups as following:

- I. MCF-7 cell line model; *MCF-7 group*: untreated MCF-7 cells used as control, *MCF-7 + DDM<sup>Plus</sup>AF group*: MCF-7 cells treated with DDM<sup>Plus</sup>AF, *MCF-7 + 6 Gy group*: MCF-7 cells treated with  $\gamma$ -rays (6 Gy-FDR) exposure, and *MCF-7 + DDM-<sup>Plus</sup>AF + 6 Gy group*: MCF-7 cells treated with DDM<sup>Plus</sup>AF and exposed to  $\gamma$ -rays 6 Gy (FDR).
- II. MDA cell line model; *MDA group*: untreated MDA-MB-231 cells used as control, *MDA + DDM<sup>Plus</sup>AF group*: MDA cells treated with DDM<sup>Plus</sup>AF, *MDA + 6 Gy group*: MDA cells treated with  $\gamma$ -rays (6 Gy-FDR) exposure, and *MDA + DDM-<sup>Plus</sup>AF + 6 Gy group*: MDA cells treated with DDM<sup>Plus</sup>AF and exposed to  $\gamma$ -rays 6 Gy (FDR).

The models start with the addition of DDM<sup>Plus</sup>AF therapy to both cell lines of BCCs, then exposed to 6 Gy-FDR (3 Gy/day for two successive days) post 24 h of DDM<sup>Plus</sup>AF therapy. Then, after 24 h incubation post last dose of radiotherapy, BCCs were harvested for the biochemical investigation of anti-cancer effect of DDM<sup>Plus</sup>AF.

### Flow cytometric analysis of the cell cycle and apoptosis

For all groups of both MCF-7 and MDA-MB-231 cell lines, after 24 h incubation post the last dose of radiotherapy, the  $3 \times 10^5$  cells/well were harvested with trypsin, washed twice in ice-cold PBS, and fixed with 70% ethanol at 4 °C overnight. Afterwards, the cells washed with PBS and collected by centrifugation, then stained by propidium-iodide (PI) (50  $\mu$ g/ml) for cell cycle analysis (Cat. No# ab139418) and using an Annexin-V-FITC Kit (Beckman Coulter, Marseille, France) for measurement of apoptosis. Staining was assessed in a FACSCanto-II flow cytometer, followed by analysis using BD Accuri-C6 Plus software (Biosciences, CA, USA) (Kojima et al. 2018).

### Tumor-promoting factors (TPF) and metabolic reprogramming measurements

The levels of tumor suppressor p53, tumor necrosis factor alpha (TNF- $\alpha$ ), interleukin 10 (IL-10), HIF-1 $\alpha$ , and ATP were determined by using enzyme-linked immunosorbent assays (ELISA) kits purchased from Sigma-Aldrich, Cat. No# RAB0500, RAB0476, RAB0244, RAB1057, and MAK190, respectively, following the manufacturers' instructions. Additionally, PRMT-1 and peroxisome proliferator-activated receptor-alpha (PPAR- $\alpha$ ) were measured using ELISA kits according to the manufacturers' instructions, Cat No #MA1-25468 and MBS269041, respectively, purchased from Thermo Fisher Scientific and MyBioSource.

The glucose and lactate metabolism in MCF-7 and MDA-MB-231 cells were measured as described in its corresponding commercial kits, Cat. No# GAGO20 and MAK064

(Sigma-Aldrich) for glucose and lactate, respectively. The glucose and lactate were determined with OD values at 540 nm and 570 nm, respectively, using a spectrophotometer.

Intracellular HK and PDH activities were evaluated with a spectrophotometer using Quantification Kit, Cat. No: MAK091-1KT and MAK183-1KT, respectively, according to the manufacturers' instructions (Merck KGaA, Darmstadt, Sigma-Aldrich, Germany). The HK and PDH concentrations were determined with OD values at 450 nm.

#### **Western blotting analysis**

MCF-7 and MDA-MB-231 cells were seeded at a density of  $4 \times 10^5$ /well in 6-well plates. After treatment, cells were lysed using lysis buffer (10  $\mu$ l PMSE, 100 mM was added to 1 ml RIPA, Solarbio, Beijing, China) on ice for 30 min. Cell lysates were separated using 10% SDS-PAGE gels and blotted on polyvinylidene difluoride membranes (PVDFMs), which were blocked with 5% skim milk in PBS containing 0.1% Tween 20 (TBST). Then, the PVDF membrane was incubated overnight with the primary antibodies at 4 °C for 12 h. The following antibodies were used: AKT (in total, 60KDa-Catalog#AHO1112, and phosphorylated form, Ser 473-55.60 KDa-Catalog#44-621G, Thermo fisher), AMPK (in total, 63KDa-Catalog #MA5-14922, and phosphorylated form, Ser485-55KDa-Catalog# PA5-117221, Thermo fisher), PGC-1 $\alpha$  (91KDa, Catalog#PA5-72948, Thermo Fisher), TGF- $\beta$  (44-53KDa, Catalog#MA5-15065, Thermo Fisher), and SIRT-1 (110 KDa, Catalog#PA5-17074, Thermo FISHER) rabbit polyclonal antibodies 1:1000, and the  $\beta$ -actin rabbit polyclonal antibodies 1:4000 (Proteintech, USA) were used as loading controls and for normalization. The secondary antibodies were anti-rabbit antibodies and were conjugated to horseradish peroxidase (1:4000; Proteintech), and were incubated for 1 h at room temperature. The bands were visualized using the ECL reagents (Thermo Fisher Scientific). Band images were obtained by using the Protein Simple Digital imaging system (Flour Chem R, USA).

#### **RNA isolation and real-time PCR analysis**

For RNA extraction, the total RNA from MCF-7 and MDA-MB-231 cells was extracted using Trizol Reagent (Thermo Fisher Scientific). cDNA was obtained from total RNA using the PrimeScript™ RT reagent kit (Takara Bio, Inc., Otsu, Japan). The expression of mRNA was assessed by qRT-PCR, which was carried out in triplicate by an SYBR Premix Ex Taq™ kit (Takara Bio, Inc.) and an ABI 7900HT Real-Time PCR system (Thermo Fisher Scientific). The primers used are FR- $\alpha$  (forward primer; CTGGCTGGTGTGGT AGAACAG and reverse primer; AGGCCCCGAGGACAAGTT) and estrogen-related receptor alpha (ERR- $\alpha$ ) (forward primer; GGCCCTTGCCAATTCAGA and reverse primer; GGCCTCGTG CAGAGCTTCT). GAPDH (forward primer; GTCAAGGCT GAGAACGGGAA and reverse primer; AAATGAGCCCCAGCCTTCTC) was used to normalize the results of qRT-PCR and the comparative cycle threshold values ( $2^{-\Delta\Delta C_t}$ ) were adopted to analyze the final results.

### Statistical analysis

All experiments were carried out at least in triplicate and the results were expressed as the mean  $\pm$  standard error of mean (SEM). The statistical analyses were performed using GraphPad Prism software (version 8, La Jolla, CA). Statistical significance between all groups was analyzed by using  $p < 0.001$ ,  $p < 0.01$  and  $p < 0.05$ .

### Supplementary Information

The online version contains supplementary material available at <https://doi.org/10.1186/s12645-022-00122-1>.

**Additional file 1: Data S1.** Stability of DDM<sup>Plus</sup>AF nanocomposites by DLS and zeta ( $\zeta$ ) potential analyses. **Data S2.** Cell survival and radio-sensitization of DDM, AF and DDM<sup>Plus</sup>AF via M-MTT assay at 24, 48 and 72h in comparison: a) MCF-7 and b) MDA cells. Data are mean  $\pm$  SEM (n = 3), where control cells are set at 100%. Columns with letter a = significant from MCF-7 or MDA cells, b = significant from MCF-7+DDM<sup>Plus</sup>AF or MDA+DDM<sup>Plus</sup>AF, c = significant from MCF-7+DDM<sup>Plus</sup>AF+3Gy or MDA+DDM<sup>Plus</sup>AF+3Gy, and d = significant from MCF-7+DDM<sup>Plus</sup>AF+6Gy or MDA+DDM<sup>Plus</sup>AF+6Gy associated with \* = significant from 24 h, # = significant from 48h and @ = significant from 72h, in each histogram at  $P < 0.05$ . **Data S3.** Diagram of DDM (a) and AF (b) synthesis.

### Acknowledgements

Not applicable.

### Author contributions

NMT: conceptualization, data curation, formal analysis, validation, investigation, visualization, methodology, writing—original draft, writing—review and editing. MKA-R: conceptualization, data curation, formal analysis, validation, investigation, visualization, methodology, writing—original draft, writing—review and editing. GSE-S: data curation, formal analysis, validation, investigation, visualization, methodology, writing—original draft, writing—review and editing. MAE-K: methodology, writing—original draft, writing—review and editing. AS: visualization, methodology, writing—original draft, writing—review and editing. Y-CD: project administration, writing—review and editing. LAR: formal analysis, validation, investigation, visualization, methodology. MAA: conceptualization, data curation, formal analysis, validation, investigation, visualization, methodology, writing—original draft, writing—review and editing. All authors read and approved the final manuscript.

### Funding

This research was funded by the Ministry of Science and Technology, Taiwan (MOST 108-2221-E-006-231-MY3 and 110-2221-E-006-087-MY3).

### Availability of data and materials

Not applicable.

### Declarations

#### Ethics approval and consent to participate

Not applicable.

#### Consent for publication

Not applicable.

#### Competing interests

The authors declare that they have no competing interests.

#### Author details

<sup>1</sup>Radiation Biology Department, National Centre for Radiation Research and Technology (NCRRT), Egyptian Atomic Energy Authority (EAEA), Cairo, Egypt. <sup>2</sup>Drug Microbiology Lab, Drug Radiation Research Department, National Centre for Radiation Research and Technology, (NCRRT), Egyptian Atomic Energy Authority (EAEA), Cairo, Egypt. <sup>3</sup>Department of Electrical and Electronic Information Engineering, Toyohashi University of Technology, Toyohashi 441-8580, Japan. <sup>4</sup>Department of Radiation Engineering, National Centre for Radiation Research and Technology (NCRRT), Egyptian Atomic Energy Authority (EAEA), Cairo, Egypt. <sup>5</sup>Department of Biomedical Engineering, National Cheng Kung University, Tainan 70105, Taiwan. <sup>6</sup>Medical Device Innovation Center, National Cheng Kung University, Tainan 70105, Taiwan. <sup>7</sup>Biochemistry Department, Kasr Alainy, Faculty of Medicine, Cairo University, Cairo, Egypt.

Received: 6 January 2022 Accepted: 5 May 2022

Published online: 28 May 2022

### References

Abdel Maksoud M, El-Sayyad GS, Ashour AH, El-Batal AI, Abd-Elmonem MS, Hendawy H, Abdel-Khalek EK, Labib S, Abdeltwab E, El-Okr MM (2018) Synthesis and characterization of metals-substituted cobalt ferrite [Mx Co(1-x) Fe2O4; (M

- = Zn, Cu and Mn;  $x = 0$  and 0.5)] nanoparticles as antimicrobial agents and sensors for Anagrelide determination in biological samples. *Mater Sci Eng C Mater Biol Appl* 92:644–656. <https://doi.org/10.1016/j.msec.2018.07.007>
- Ahamed M, Alhadiq HA, Khan MAM, Akhtar MJ (2013) Selective killing of cancer cells by iron oxide nanoparticles mediated through reactive oxygen species via p53 pathway. *J Nanopart Res* 15:1225. <https://doi.org/10.1007/s11051-012-1225-6>
- Angelopoulou A, Kolokithas-Ntoukas A, Fytas C, Avgoustakis K (2019) Folic acid-functionalized, condensed magnetic nanoparticles for targeted delivery of doxorubicin to tumor cancer cells overexpressing the folate receptor. *ACS Omega* 4(26):22214–22227. <https://doi.org/10.1021/acsomega.9b03594>
- Antonosante A, d'Angelo M, Castelli V, Catanesi M, Iannotta D, Giordano A, Ippoliti R, Benedetti E, Cimini A (2018) The Involvement of PPARs in the peculiar energetic metabolism of tumor cells. *Int J Mol Sci* 19(7):1907. <https://doi.org/10.3390/ijms19071907>
- Ashour A, El-Batal AI, AbdelMaksoud MIA, El-Sayyad GS, Labib Sh, Abdeltwab E, El-Okr MM (2018) Antimicrobial activity of metal-substituted cobalt ferrite nanoparticles synthesized by sol-gel technique. *Particuology* 40:141–151. <https://doi.org/10.1016/j.Partic.2017.12.001>
- Azmat R, Pervaiz A, Masood S (2020) Synthesis, characterization, and activity of maghemite ( $\gamma$ -Fe<sub>2</sub>O<sub>3</sub>) nanoparticles through a facile solvent hydrothermal phase transformation of Fe<sub>2</sub>O<sub>3</sub>. In: Bhargava C, Sachdeva A, Bhargava C, Sachdeva A (eds) *Nanotechnology*, 1st edn. CRC Press, Boca Raton, pp 277–294
- Balakrishnan GV, Batook M, Raslan EH (2020) Microstructure, optical and photocatalytic properties of MgO nanoparticles. *Results Phys* 16:103013. <https://doi.org/10.1016/j.rinp.2020.103013>
- Baldwin RM, Moretini A, Côté J (2014) Role of PRMTs in cancer: could minor isoforms be leaving a mark? *World J Biol Chem* 5(2):115–129. <https://doi.org/10.4331/wjbc.v5.i2.115>
- Baskar R, Dai J, Wenlong N, Yeo R, Yeoh KW (2014) Biological response of cancer cells to radiation treatment. *Front Mol Biosci* 1:24. <https://doi.org/10.3389/fmolb.2014.00024>
- Behzadi E, Sarsharzadeh R, Nouri M, Attar F, Akhtari K, Shahpasand K, Falahati M (2019) Albumin binding and anti-cancer effect of magnesium oxide nanoparticles. *Int J Nanomed* 14:257–270. <https://doi.org/10.2147/IJN.S186428>
- Belavi P, Chavan GN, Naik LR, Somashekar R, Kotnala RK (2012) Structural, electrical and magnetic properties of cadmium substituted nickel-copper ferrites. *Mater Chem Phys* 132(1):138–144. <https://doi.org/10.1016/j.matchemphys.2011.11.009>
- Bonn M, Hunger J (2021) Between a hydrogen and a covalent bond. *Science* 371(6525):123–124. <https://doi.org/10.1126/science.abf3543>
- Buch K, Peters T, Nawroth T, Sängler M, Schmidberger H, Langguth P (2012) Determination of cell survival after irradiation via clonogenic assay versus multiple MTT assay—a comparative study. *Radiat Oncol* 7:1. <https://doi.org/10.1186/1748-717X-7-1>
- Cao H, Wen G, Li H (2014) Role of peroxisome proliferator activated receptor  $\alpha$  in atherosclerosis. *Mol Med Rep* 9(5):1755–1760. <https://doi.org/10.3892/mmr.2014.2020>
- Cazares-Cortes E, Espinosa A, Guigner JM, Michel A, Griffete N, Wilhelm C, Ménager C (2017) Doxorubicin intracellular remote release from biocompatible oligo(ethylene glycol) methyl ether methacrylate-based magnetic nanogels triggered by magnetic hyperthermia. *ACS Appl Mater Interfaces* 9(31):25775–25788. <https://doi.org/10.1021/acsami.7b06553>
- de Oliveira SA, da Silva BC, Riegel-Vidotti IC, Urbano A, de Sousa F-T, Tischer CA (2017) Production and characterization of bacterial cellulose membranes with hyaluronic acid from chicken comb. *Int J Biol Macromol* 97:642–653. <https://doi.org/10.1016/j.ijbiomac.2017.01.077>
- Deng C-X (2009) SIRT1, is it a tumor promoter or tumor suppressor? *Int J Biol Sci* 5(2):147–152. <https://doi.org/10.7150/ijbs.5.147>
- Deng X, Li Y, Gu S, Chen Y, Yu B, Su J, Sun L, Liu Y (2020) p53 affects PGC1 $\alpha$  stability through AKT/GSK-3 $\beta$  to enhance cisplatin sensitivity in non-small cell lung cancer. *Front Oncol* 10:1252. <https://doi.org/10.3389/fonc.2020.01252>
- Diana P, Saravanakumar S, Prasad KH, Sivaganesh D, Chidhambaram N, Rimal IRS, Alshahrani T, Shkir M, AlFaify S, Ali KSS (2021) Enhanced photocatalytic decomposition efficacy of novel MgO NPs: impact of annealing temperatures. *J Inorg Organomet Polym* 31:3027–3036. <https://doi.org/10.1007/s10904-021-01896-4>
- Dias AS, Almeida CR, Helguero LA, Duarte IF (2019) Metabolic crosstalk in the breast cancer microenvironment. *Eur J Cancer* 121:154–171. <https://doi.org/10.1016/j.ejca.2019.09.002>
- Dukhinova MS, Prilepskii AY, Shtil AA, Vinogradov VV (2019) Metal oxide nanoparticles in therapeutic regulation of macrophage functions. *Nanomaterials* 9(11):1631. <https://doi.org/10.3390/nano9111631>
- El-Batal AI, Al-Hazim NE, Farrag AA, Elsayed MA, EL-Khawaga AM, El-Sayyad GS, Elshamy AA (2022) Antimicrobial synergism and antibiofilm activity of amoxicillin loaded citric acid-magnesium ferrite nanocomposite: Effect of UV-illumination, and membrane leakage reaction mechanism. *Microb Pathog* 164:105440. <https://doi.org/10.1016/j.micpath.2022.105440>
- El-Desouky MA, Fahmi AA, Abdelkader IY, Nasraddin KM (2020) Anticancer effect of amygdalin (vitamin B-17) on hepatocellular carcinoma cell line (HepG2) in the presence and absence of zinc. *Anticancer Agents Med Chem* 20(4):486–494. <https://doi.org/10.2174/1871520620666200120095525>
- Espinosa A, Di Corato R, Kolosnjaj-Tabi J, Flaud P, Pellegrino T, Wilhelm C (2016) Duality of iron oxide nanoparticles in cancer therapy: amplification of heating efficiency by magnetic hyperthermia and photothermal bimodal treatment. *ACS Nano* 10(2):2436–2446. <https://doi.org/10.1021/acsnano.5b07249>
- Fouad DE, Zhang C, El-Didamony H, Yingnan L, Mekuria TD, Shah AH (2019) Improved size, morphology and crystallinity of hematite ( $\alpha$ -Fe<sub>2</sub>O<sub>3</sub>) nanoparticles synthesized via the precipitation route using ferric sulfate precursor. *Results Phys* 12:1253–1261. <https://doi.org/10.1016/j.Rinp.2019.01.005>
- Garg UK, Kaur MP, Garg VK, Sud D (2007) Removal of hexavalent chromium from aqueous solution by agricultural waste biomass. *J Hazard Mater* 140(1–2):60–68. <https://doi.org/10.1016/j.jhazmat.2006.06.056>
- Grabacka M, Reiss K (2008) Anticancer properties of PPAR $\alpha$ -effects on cellular metabolism and inflammation. *PPAR Res* 2008:930705. <https://doi.org/10.1155/2008/930705>

- Guo Y, Xu H, Li Y, Wu F, Li Y, Bao Y, Yan X, Huang Z, Xu P (2017) Hyaluronic acid and Arg-Gly-Asp peptide modified graphene oxide with dual receptor-targeting function for cancer therapy. *J Biomater Appl* 32(1):54–65. <https://doi.org/10.1177/0885328217712110>
- Han X, Guo B, Li Y, Zhu B (2014) Tissue factor in tumor microenvironment: a systematic review. *J Hematol Oncol* 1(7):54. <https://doi.org/10.1186/s13045-014-0054-8>
- Harbeck N, Gnant M (2017) Breast cancer. *Lancet* 389(10074):1134–1150. [https://doi.org/10.1016/S0140-6736\(16\)31891-8](https://doi.org/10.1016/S0140-6736(16)31891-8)
- He YY, Wang XC, Jin PK, Zhao B, Fan X (2009) Complexation of anthracene with folic acid studied by FTIR and UV spectroscopies. *Spectrochim Acta Part A Mol Biomol Spectrosc* 72(4):876–879. <https://doi.org/10.1016/j.saa.2008.12.021>
- Hua W, Ten Dijke P, Kostidis S, Giera M, Hornsveld M (2020) TGF $\beta$ -induced metabolic reprogramming during epithelial-to-mesenchymal transition in cancer. *Cell Mol Life Sci* 77(11):2103–2123. <https://doi.org/10.1007/s00018-019-03398-6>
- Ip W, Hoshi N, Shouval DS, Snapper S, Medzhitov R (2017) Anti-inflammatory effect of IL-10 mediated by metabolic reprogramming of macrophages. *Science* 356(6337):513–519. <https://doi.org/10.1126/science.aal3535>
- ISO/ASTM E 51026 (2015) Practice for using the fricke dosimeter system. ASTM international, west Conshohocken, PA. <https://www.astm.org/e1026-15.html>
- James MO, Jahn SC, Zhong G, Smeltz MG, Hu Z, Stacpoole PW (2017) Therapeutic applications of dichloroacetate and the role of glutathione transferase zeta-1. *Pharmacol Ther* 170:166–180. <https://doi.org/10.1016/j.pharmthera.2016.10.018>
- Janic B, Liu F, Bobbitt KR, Brown SL, Chetty IJ, Mao G, Movsas B, Wen N (2018) Cellular uptake and radio-sensitization effect of small gold nanoparticles in MCF-7 breast cancer cells. *J Nanomed Nanotechnol* 9(2):1–13
- Jaszczak-Wilke E, Polkowska Z, Koprowski M, Owsianik K, Mitchell AE, Balczewski P (2021) Amygdalin: toxicity, anticancer activity and analytical procedures for its determination in plant seeds. *Molecules* 26(8):2253. <https://doi.org/10.3390/molecules26082253>
- Jin S, Du Z, Wang P, Guo H, Zhang H, Lei X, Ren F (2019) 2-Deoxyglucose-modified folate derivative: self-assembling nanoparticle able to load cisplatin. *Molecules* 24(6):1084. <https://doi.org/10.3390/molecules24061084>
- Jurczyk M, Jelonek K, Musiał-Kulik M, Beberok A, Wrześniak D, Kasperczyk J (2021) Single- versus dual-targeted nanoparticles with folic acid and biotin for anticancer drug delivery. *Pharmaceutics* 13(3):326. <https://doi.org/10.3390/pharmaceutics13030326>
- Karade VC, Parit SB, Dawkar VV, Devan RS, Choudhary RJ, Kedge VV, Pawar NV, Kim JH, Chougale AD (2019) A green approach for the synthesis of  $\alpha$ -Fe $_2$ O $_3$  nanoparticles from *Gardenia resinifera* plant and its in vitro hyperthermia application. *Heliyon* 5(7):e02044. <https://doi.org/10.1016/j.heliyon.2019.e02044>
- Kojima K, Takahashi S, Saito S, Endo Y, Nittami T, Nozaki T, Sobti RC, Watanabe M (2018) Combined effects of Fe $_3$ O $_4$  nanoparticles and chemotherapeutic agents on prostate cancer cells in vitro. *Appl Sci* 8(1):134. <https://doi.org/10.3390/app8010134>
- Lee Y-K, Park OJ (2011) Involvement of AMPK/mTOR/HIF-1 $\alpha$  in anticancer control of quercetin in hypoxic MCF-7 cells. *Food Sci Biotechnol* 20(2):371–375
- Liang T, Xiaogang G, Binfang Y, Shuying K, Huisheng H, Daoling Fu, Fulan Z, Jianhua X, Xueming L (2020) Design of functionalized  $\alpha$ -Fe $_2$ O $_3$  (III) films with long-term anti-wetting properties. *Ceram Int* 46(5):6129–6135. <https://doi.org/10.1016/j.ceramint.2019.11.077>
- Liczbiński P, Bukowska B (2018) Molecular mechanism of amygdalin action in vitro: review of the latest research. *Immunopharmacol Immunotoxicol* 40(3):212–218. <https://doi.org/10.1080/08923973.2018.1441301>
- Liu J, Xiao HT, Wang HS, Mu HX, Zhao L, Du J, Yang D, Wang D, Bian ZX, Lin SH (2016) Halofuginone reduces the inflammatory responses of DSS-induced colitis through metabolic reprogramming. *Mol Biosyst* 12(7):2296–2303. <https://doi.org/10.1039/c6mb00154h>
- Liu M, Wang B, Guo C, Hou X, Cheng Z, Chen D (2019) Novel multifunctional triple folic acid, biotin and CD44 targeting pH-sensitive nano-actiniae for breast cancer combinational therapy. *Drug Deliv* 26(1):1002–1016. <https://doi.org/10.1080/10717544.2019.1669734>
- Luo Z, Qin C, Wu Y, Wenjing X, Zhang S, Lu A (2020) Structure and properties of Fe $_2$ O $_3$ -doped 50Li $_2$ O-10B $_2$ O $_3$ -40P $_2$ O $_5$  glass and glass-ceramic electrolytes. *Solid State Ionics* 345:115177. <https://doi.org/10.1016/j.ssi.2019.115177>
- Maksoud M, El-Sayyad GS, Ashour AH, El-Batal AI, Elsayed MA, Gobara M, El-Khawaga AM, Abdel-Khalek EK, El-Okr MM (2019) Antibacterial, antibiofilm, and photocatalytic activities of metals-substituted spinel cobalt ferrite nanoparticles. *Microb Pathog* 127:144–158. <https://doi.org/10.1016/j.micpath.2018.11.045>
- Mazur CM, Tate JA, Strawbridge RR, Gladstone DJ, Hoopes PJ (2013) Iron oxide nanoparticle enhancement of radiation cytotoxicity. *Proc SPIE Int Soc Opt Eng* 8584:85840J. <https://doi.org/10.1117/12.2007701>
- Mi Y, Shao Z, Vang J, Kaidar-Person O, Wang AZ (2016) Application of nanotechnology to cancer radiotherapy. *Cancer Nanotechnol* 7(1):11. <https://doi.org/10.1186/s12645-016-0024-7>
- Minafra L, Porcino N, Bravatà V, Gaglio D, Bonanomi M, Amore E, Cammarata FP, Russo G, Militello C, Savoca G, Baglio M, Abbate B, Iacoviello G, Evangelista G, Gilardi MC, Bondi ML, Forte GI (2019) Radiosensitizing effect of curcumin-loaded lipid nanoparticles in breast cancer cells. *Sci Rep* 9(1):11134. <https://doi.org/10.1038/s41598-019-47553-2>
- Mohammed E-D (2014) Qualitative and quantitative determination of folic acid in tablets by FTIR spectroscopy. *IJAPBC* 3:773–780
- Moldogazieva NT, Mokhosoev IM, Terentiev AA (2020) Metabolic heterogeneity of cancer cells: an interplay between HIF-1, GLUTs, and AMPK. *Cancers* 12(4):62. <https://doi.org/10.3390/cancers12040862>
- Najim SS (2017) Determination of some trace elements in breast cancer serum by atomic absorption spectroscopy. *Int J Chem* 9:1–6. <https://doi.org/10.5539/ijc.v9n1p1>
- Nasser H, El-Naggar S, El-Sayed Rizk M, Elmetwalli A, Salama A (2021) Effect of sorafenib on liver biochemistry prior to vitamin B17 Coadministration in ehrlich ascites carcinoma mice model: preliminary phase study. *Biochem Lett* 17(1):40–49. <https://doi.org/10.21608/blj.2021.184392>
- Owusu BY, Gallema R, Janetka J, Klampfer L (2017) Hepatocyte growth factor, a key tumor-promoting factor in the tumor microenvironment. *Cancers* 9:35. <https://doi.org/10.3390/cancers9040035>
- Pajak B, Siviak E, Sołyka M, Priebe A, Zieliński R, Fokt I, Ziemniak M, Jaśkiewicz A, Borowski R, Domoradzki T, Priebe W (2019) 2-Deoxy-D-glucose and its analogs: from diagnostic to therapeutic agents. *Int J Mol Sci* 21(1):234. <https://doi.org/10.3390/ijms21010234>

- Perillo B, Di Donato M, Pezone A, Di Zazzo E, Giovannelli P, Galasso G, Castoria G, Migliaccio A (2020) ROS in cancer therapy: the bright side of the moon. *Exp Mol Med* 52(2):192–203. <https://doi.org/10.1038/s12276-020-0384-2>
- Planeta K, Kubala-Kukus A, Drozd A, Matusiak K, Setkowicz Z, Chwiej J (2021) The assessment of the usability of selected instrumental techniques for the elemental analysis of biomedical samples. *Sci Rep* 11(1):3704. <https://doi.org/10.1038/s41598-021-82179-3>
- Puzio-Kuter AM (2011) The role of p53 in metabolic regulation. *Genes Cancer* 2(4):385–391. <https://doi.org/10.1177/1947601911409738>
- Pyaskovskaya ON, Kolesnik DL, Fedorchuk AG, Prokhorova IV, Solyanik GI (2016) 2-Deoxy-D-glucose enhances dichloroacetate antitumor action against Lewis lung carcinoma. *Exp Oncol* 38(3):176–180
- Reddy KJ, Karunakaran K (2013) Purification and characterization of hyaluronic acid produced by *Streptococcus zooepidemicus* strain 3523-7. *J BioSci Biotechnol* 2(3):173–179
- Reheem AA, Atta A, Maksoud MA (2016) Low energy ion beam induced changes in structural and thermal properties of polycarbonate. *Radiat Phys Chem* 127:269–275. <https://doi.org/10.1016/j.radphyschem.2016.07.014>
- Revia RA, Zhang M (2016) Magnetite nanoparticles for cancer diagnosis, treatment, and treatment monitoring: recent advances. *Mater Today* 19(3):157–168. <https://doi.org/10.1016/j.mattod.2015.08.022>
- Sankadiya S, Oswal N, Jain P, Gupta N (2016) Synthesis and characterization of Fe<sub>2</sub>O<sub>3</sub> nanoparticles by simple precipitation method. *AIIP Conf Proc*. <https://doi.org/10.1063/1.4945184>
- Sharma M (2017)  $\alpha$ -Fe<sub>2</sub>O<sub>3</sub> preparation by Sol–Gel method. <https://document.org/document/fe2o3-preparation-by-sol-gel-method-2017-9-27-fe-2o-3-manas-sharma-1-objective.html>
- Shebanova ON, Lazor P (2003) Raman spectroscopic study of magnetite (FeFe<sub>2</sub>O<sub>4</sub>): a new assignment for the vibrational spectrum. *J Solid State Chem* 174(2):424–430. [https://doi.org/10.1016/S0022-4596\(03\)00294-9](https://doi.org/10.1016/S0022-4596(03)00294-9)
- Shi R, Tang YQ, Miao H (2020) Metabolism in tumor microenvironment: implications for cancer immunotherapy. *MedComm* 1(1):47–68. <https://doi.org/10.1002/mco.26>
- Shiratori R, Furuichi K, Yamaguchi M, Miyazaki N, Aoki H, Chibana H, Ito K, Aoki S (2019) Glycolytic suppression dramatically changes the intracellular metabolic profile of multiple cancer cell lines in a mitochondrial metabolism-dependent manner. *Sci Rep* 9(1):18699. <https://doi.org/10.1038/s41598-019-55296-3>
- Tadic M, Panjan M, Tadic B, Lazovic J, Damjanovic V, Kopani M, Kopanja L (2019) Magnetic properties of hematite ( $\alpha$ -Fe<sub>2</sub>O<sub>3</sub>) nanoparticles synthesized by sol-gel synthesis method: the influence of particle size and particle size distribution. *J Electr Eng* 70(7):71–76. <https://doi.org/10.2478/jee-2019-0044>
- Tan Z, Luo X, Xiao L, Tang M, Bode AM, Dong Z, Cao Y (2016) The role of PGC1 $\alpha$  in cancer metabolism and its therapeutic implications. *Mol Cancer Ther* 15(5):774–782. <https://doi.org/10.1158/1535-7163.MCT-15-0621>
- Tang L, Wei F, Wu Y, He Y, Shi L, Xiong F, Gong Z, Guo C, Li X, Deng H, Cao K, Zhou M, Xiang B, Li X, Li Y, Li G, Xiong W, Zeng Z (2018) Role of metabolism in cancer cell radioresistance and radiosensitization methods. *J Exp Clin Cancer Res* 37(1):87. <https://doi.org/10.1186/s13046-018-0758-7>
- Thakur A, Vaidya D, Kaushal M, Gupta A (2019) Physicochemical properties, mineral composition, FTIR spectra and scanning electron microscopy of wild apricot kernel press cake. *Int J Food Sci Nutr* 4(2):140–143
- Uppuluri S, Swanson DR, Piehler LT, Li J, Hagnauer GL, Tomalia DA (2000) Core–shell tecto (dendrimers): I. Synthesis and characterization of saturated shell models. *Adv Mater* 12(11):796–800. [https://doi.org/10.1002/\(SICI\)1521-4095\(200006\)12:11%3C796::AID-ADMA796%3E3.0.CO;2-1](https://doi.org/10.1002/(SICI)1521-4095(200006)12:11%3C796::AID-ADMA796%3E3.0.CO;2-1)
- Vamecq J, Colet JM, Vanden Eynde JJ, Briand G, Porchet N, Rocchi S (2012) PPARs: interference with Warburg effect and clinical anticancer trials. *PPAR Res* 2012:304760. <https://doi.org/10.1155/2012/304760>
- van de Loosdrecht AA, Beelen RH, Ossenkoppele GJ, Broekhoven MG, Langenhuijsen MM (1994) A tetrazolium-based colorimetric MTT assay to quantitate human monocyte mediated cytotoxicity against leukemic cells from cell lines and patients with acute myeloid leukemia. *J Immunol Methods* 174(1–2):311–320. [https://doi.org/10.1016/0022-1759\(94\)90034-5](https://doi.org/10.1016/0022-1759(94)90034-5)
- Vaughan RA, Garcia-Smith R, Dorsey J, Griffith JK, Bisoffi M, Trujillo KA (2013) Tumor necrosis factor alpha induces Warburg-like metabolism and is reversed by anti-inflammatory curcumin in breast epithelial cells. *Int J Cancer* 133(10):2504–2510. <https://doi.org/10.1002/ijc.28264>
- Vinardell MP, Mitjans M (2015) Antitumor activities of metal oxide nanoparticles. *Nanomaterials* 5(2):1004–1021. <https://doi.org/10.3390/nano5021004>
- Wang J-s, Wang H-j, Qian H-I (2018) Biological effects of radiation on cancer cells. *Mil Med Res* 5(1):1–10. <https://doi.org/10.1186/s40779-018-0167-4>
- Whiteside T (2008) The tumor microenvironment and its role in promoting tumor growth. *Oncogene* 27:5904–5912. <https://doi.org/10.1038/onc.2008.271>
- Wrzesinski K, Fey SJ (2018) Metabolic reprogramming and the recovery of physiological functionality in 3D cultures in micro-bioreactors. *Bioengineering* 5(1):22. <https://doi.org/10.3390/bioengineering5010022>
- Yang C, Wu T, Qin Y, Qi Y, Sun Y, Kong M, Jiang X, Qin X, Shen Y, Zhang Z (2018) A facile doxorubicin-dichloroacetate conjugate nanomedicine with high drug loading for safe drug delivery. *Int J Nanomed* 13:1281–1293. <https://doi.org/10.2147/IJN.S154361>
- Zeng QZ, Ma SY, Jin WX, Yang HM, Chen H, Ma QG (2017) Hydrothermal synthesis of monodisperse  $\alpha$ -Fe<sub>2</sub>O<sub>3</sub> hollow microspheroids and their high gas-sensing properties. *J Alloy Compd* 705:427–437. <https://doi.org/10.1016/j.jallcom.2017.01.268>
- Zhao Y, Butler EB, Tan M (2013) Targeting cellular metabolism to improve cancer therapeutics. *Cell Death Dis* 4(3):e532–e532. <https://doi.org/10.1038/cddis.2013.60>
- Zipare K, Bandgar S, Shahane G (2018) Effect of Dy-substitution on structural and magnetic properties of MnZn ferrite nanoparticles. *J Rare Earths* 36(1):86–94. <https://doi.org/10.1016/j.jre.2017.06.011>

## Publisher's Note

Springer Nature remains neutral with regard to jurisdictional claims in published maps and institutional affiliations.